A Dynamic Thermodynamic Sea Ice Model

W. D. HIBLER III[1]

U.S. Army Cold Regions Research and Engineering Laboratory, Hanover, NH 03755

(Manuscript received 1 May 1978, in final form 13 December 1978)

ABSTRACT

A numerical model for the simulation of sea ice circulation and thickness over a seasonal cycle is presented. This model is used to investigate the effects of ice dynamics on Arctic ice thickness and air-sea heat flux characteristics by carrying out several numerical simulations over the entire Arctic Ocean region. The essential idea in the model is to couple the dynamics to the ice thickness characteristics by allowing the ice interaction to become stronger as the ice becomes thicker and/or contains a lower areal percentage of thin ice. The dynamics in turn causes high oceanic heat losses in regions of ice divergence and reduced heat losses in regions of convergence. To model these effects consistently the ice is considered to interact in a plastic manner with the plastic strength chosen to depend on the ice thickness and concentration. The thickness and concentration, in turn, evolve according to continuity equations which include changes in ice mass and percent of open water due to advection, ice deformation and thermodynamic effects.

For the standard experiment an integration of eight years in length is performed at one day timesteps and 125 km resolution in order to obtain a cyclic equilibrium. A zero ice strength condition is used at the Greenland-Spitsbergen passage to allow natural outflow or inflow. Several other shorter experiments, including a case without open water effects, are also run for comparison. Input fields consist of observed time varying geostrophic winds over a one year period, fixed geostrophic ocean currents, and geographically invariant ice growth rates dependent on ice thickness and season.

Many of the observed features of the circulation and thickness of the Arctic ice cover are reproduced by the model. The average annual drift shows the classic anticyclonic ice flow in the Beaufort Sea together with a transpolar drift of ice from the Siberian coast toward the Greenland Sea. In addition, the nonlinear plastic rheology allows the formation of a shear zone (velocity discontinuity) from time to time off the North Slope of Alaska. The average rate of ice export out of the basin is ~0.1 Sv in reasonable agreement with observational estimates. Geographical ice thickness contours show ice in excess of 6 m along the Canadian Archipelago with thicknesses decreasing to 2 m near the Siberian coast. The form of these contours is in good agreement with that estimated from submarine sonar data and aerial ridge surveys. In summer a low compactness region of up to 50% open water builds up off the Alaskan and Siberian coasts, in general agreement with satellite-derived ice concentration charts. Further from shore, smaller, but still significant, amounts (~10%) of open water also form in summer. An important, less verifiable characteristic is that the annual net ice production is dominated by the North Slope and Siberian nearshore regions where, on the average, offshore advection creates open water and thinner ice. Overall the simulation results suggest that lateral heat transport due to ice motion is of the same order of magnitude as vertical air-sea heat fluxes.

1. Introduction

In the polar regions the interaction between the atmosphere and the oceans is significantly affected by both the dynamic and thermodynamic characteristics of sea ice. Numerical studies examining the role of sea ice in climatic change to date (e.g., Maykut and Untersteiner, 1971; Semtner, 1976a; Washington *et al.*, 1976; Bryan *et al.*, 1975; Parkinson and Washington, 1979; Manabe *et al.*, 1979) have primarily emphasized the thermodynamic characteristics, and have concentrated on properly estimating the heat flux through an ice cover of constant thickness with possibly a certain fraction of leads. While some of these studies have included transport effects (e.g., Bryan *et al.*, 1975; Parkinson and Washington, 1979; Manabe *et al.*, 1979) the dynamics and the resultant opening and closing of leads have been treated in only a simplified ad hoc manner. In particular, none of these studies have made use of a well-defined rheology relating ice deformation and thickness to the internal stresses in the ice cover. As a step toward remedying this situation, this paper discusses the development and numerical testing of a more general sea ice model in which the strength of the ice interaction is related to the ice thickness characteristics by means of a plastic rheology. In this work, emphasis

[1] Work performed while on leave as a Visiting Fellow, Geophysical Fluid Dynamics Program, Princeton University, Princeton, NJ 08540.

has been placed on developing a model suitable for seasonal simulations over large regions, and hence usable in numerical investigations of climate.

In an ice-covered ocean, rates of freezing depend on the distribution of ice thicknesses and open water present in any one area which, in turn, are dependent on the ice transport patterns. On the other hand, the ice transport is modified by the ice thicknesses and open water which determine the amount of stress the ice can transmit. In a dynamic thermodynamic model these two effects are coupled by allowing the ice interaction to depend on the ice thickness and fraction of open water, which, in turn, are functions of both the thermodynamics and dynamics.

Previous studies examining the effects of ice interaction have usually emphasized the dynamics only. The ice circulation over the whole Arctic Ocean has been examined by Felzenbaum (1958) using free drift calculations (no ice interaction) based on the mean annual geostrophic wind and currents. The same input fields were used in subsequent examinations by Campbell (1965), who assumed a Newtonian viscous ice interaction, and by Rothrock (1975a) who assumed the ice was incompressible. Studies by Hibler (1974) and Hibler and Tucker (1979) examined drift and deformation results far from shore using a linear viscous model with idealized boundary conditions. Nearshore studies off the North Slope of Alaska have been done by Pritchard (1978) using different plastic rheologies. In all these studies ice drift has been calculated without any coupling to ice thickness.

Utilization of a coupled dynamic thermodynamic model allows a more general simulation to be carried out. By integrating such a model over sufficiently long time intervals (several years) results for both drift and thickness can be obtained which are relatively independent of initial conditions. While a number of short-term integrations of such coupled models have been done for localized regions [most notably in conjunction with the AIDJEX Program (e.g., Coon *et al.*, 1976; Pritchard *et al.*, 1977)] less work has been done on a simulation to cyclic (annual) equilibrium. To the author's knowledge, the present study is the first attempt to use such a coupled model to carry out a long-term equilibrium simulation of the ice cover of the Arctic Ocean.

Such an equilibrium simulation over a seasonal cycle allows a comparison to be made to considerable data in addition to drift and deformation results. In particular, comparisons may be made to ice thickness contours estimated from submarine sonar data and aerial ridge surveys, ice concentration estimates taken from satellite imagery, observationally estimated mass balance statistics, the extent of the reduction of the ice interaction strength in summer, and the formation of a shear zone off the North Slope of Alaska. In addition, such a study yields insight into certain poorly documented climatic characteristics such as the geographical variation in sea air heat fluxes. The primary purpose of this paper is to show that many of these observed arctic ice circulation and thickness characteristics can be simulated by including the effects of ice interaction in a coupled dynamic thermodynamic model. For this purpose relatively idealized thermodynamics and a simplified ice thickness distribution have been used to be superseded by more complete parameterizations in further work.

2. Description of the model

a. Outline of essential features

The model described here is patterned after the model developed by Coon *et al.* (1974) in conjunction with the Arctic Ice Dynamics Joint Experiment (AIDJEX). The model is not as detailed as the AIDJEX formulation [for a review see Coon (1979)], but is a more practical design which allows larger time steps and a simpler treatment of boundaries. Here, particular emphasis was placed on developing a model suitable for long-term simulations, which are relevant to climatic studies. A notable feature of this work is the development of a viscous-plastic constitutive law, which allows nonlinear plastic flow to be modeled without severe time step limitations. The components of the model are a *momentum balance* which includes air and water stresses, Coriolis force, internal ice stress, inertial forces and ocean tilt; a *constitutive law* which relates the ice stress to the strain rate and the ice strength; a simple *ice thickness distribution* (consisting of the fraction of open water and the total ice mass) which accounts for the change of ice thickness and concentration due to growth or ablation, advection and deformation; and an *ice strength* determined as a function of the ice thickness and fraction of open water.

Probably the most important aspect of this model is the constitutive law which describes the nature of the ice interaction. Previous seasonal simulations have used ad hoc velocity corrections to approximate this interaction. In particular, in calculations using a global atmosphere ocean model, Bryan *et al.* (1975) and Manabe *et al.* (1979) allow the sea ice to drift with the upper ocean until it reaches a fixed cutoff thickness. When this occurs, its motion is totally stopped. In a simulation using climatological input data, Parkinson and Washington (1979) correct iteratively the free drift ice velocity field (obtained by neglecting the ice interaction) to insure the maintenance of a fixed fraction of leads. This iterative procedure, however, is performed without regard to conservation of momen-

tum, and in practice appears to stop all motion rather than modify the relative motion as occurs in reality.

A more consistent way to treat the ice interaction is to use a rheology employing a constitutive law relating the ice deformation and thickness to the internal stresses in the ice cover. Various studies associated with the AIDJEX program have indicated that rate-independent plastic rheologies seem most appropriate for describing sea ice. The idea in these plastic rheologies is to allow equivalent stresses to occur in the ice pack for both small and large deformation rates. This is in contrast to linear viscous rheologies where stresses are proportional to the deformation rate (for a one-dimensional example see Fig. 1). In addition, by using such a rheology it is possible to allow the ice to strongly resist compressive and shearing deformation, while allowing dilation (opening) to occur with little or no stress.

In order to model plastic behavior Coon *et al.* (1974) consider the ice to be an elastic-plastic continuum in which, for certain strain states, the ice behaves elastically. However, inclusion of the elasticity necessitates keeping track of the strain state of a given portion of ice indefinitely (which usually forces a Lagrangian formulation). Moreover, the mathematical complexities inherent in keeping track of the elastic behavior are substantial—both theoretically (Pritchard, 1975) and numerically (Colony and Pritchard, 1975).

To avoid these complexities, while still retaining plastic behavior under flow, sea ice is here considered to be a nonlinear viscous compressible fluid. In this more conventional fluid approach, the nonlinear viscosities are adjusted so that the ice interacts in a rigid-plastic manner for normal deformation rates and as a linear viscous fluid, with a pressure term, for very small deformation rates. Use of this viscous-plastic approach allows the essential features of plastic flow to be modeled without time step limitations (by means of implicit numerical techniques) and facilitates an Eulerian formulation.

A comparison, in the one-dimensional case, between this viscous-plastic approach, the elastic-plastic method and linear viscosity is illustrated in Fig. 1. In the elastic-plastic case the material resists compression with a fixed stress, once a certain converging deformation has occurred, and has no resistance to diverging strains. In the viscous-plastic case similar behavior occurs except that the stress state is determined by the magnitude of the strain rate rather than the strain. The important difference between both plastic approaches and linear viscosity is that the stresses are large even for small strain rates and independent of the rate of deformation (except for very small rates). More

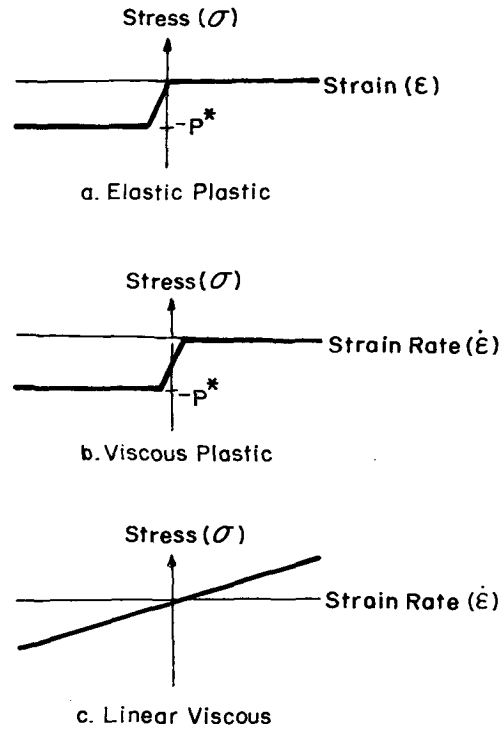

FIG. 1. One-dimensional comparison of elastic-plastic, viscous-plastic and linear viscous rheologies. Note that the viscous-plastic rheology may be considered to be a nonlinear viscous fluid with a pressure term: $\sigma = \eta\dot{\epsilon} - 0.5P^*$, where η is the minimum $(0.5P^*/|\epsilon|, \dot{\epsilon}_0)$ with $\dot{\epsilon}_0$ a constant.

detailed justifications for such rate independent behavior are discussed by Rothrock (1975b) and Coon (1979).

An essential difference between the viscous-plastic law and the elastic-plastic law is the way in which relatively motionless situations are treated. In the elastic-plastic case a high stress can be maintained in such cases without any relative ice motion by allowing the ice to behave elastically. In the viscous-plastic case such "rigid" cases are approximated by a state of very slow flow, or creep. Which closure scheme is more physically realistic remains to be seen. However, for most applications this question is moot. In particular, by making the strain rates for the onset of plastic behavior very small, the amount of creep occurring in a viscous-plastic simulation can be effectively made negligible.

The other important aspects of the model are an ice thickness distribution and a relationship between this thickness distribution and the strength of the ice interaction. A framework for dealing with such a variable ice thickness has been formulated by Thorndike *et al.* (1975), who introduced an areal ice thickness distribution (fraction of area covered by ice of a given thickness), and developed equations for the dynamic thermodynamic evolu-

tion of this distribution. To couple the ice thickness distribution with the ice strength, Rothrock (1975b) suggested that the rate of work done on the ice through ridging might be related to the work done by the ice interaction forces.

For the model described here a simplification of the Thorndike-Rothrock approach is developed. In particular, only two categories of ice are considered: thin and thick. The thin ice is characterized by a certain areal fraction of open water, while the thick ice, covering the remaining area, is taken to be of constant thickness for growth rate estimates. The effect of ice dynamics on the thin ice is parameterized by allowing, in addition to advection, open water to be formed under diverging ice conditions and to be removed for converging conditions. To parameterize the effect of thermodynamics on thin ice, the fraction of open water is taken to decrease under growth conditions and increase under melting conditions. In addition, the total ice mass at any given point is taken to obey continuity requirements with the mass increasing under growth (by the combined ice formed over the open water and the thick ice) and decreasing under melting conditions. To relate the ice interaction to the variable ice thickness the ice strength is taken to be a simple function of the ice thickness and open water.

The modifications to the Thorndike-Rothrock approach developed here are not considered fundamental changes. Rather, they are considered to be useful simplifications which facilitate interpretation of the simulation results and were felt to be adequate for this particular study. Moreover, while relatively simple, the parameterization proposed here does capture many features of the variable thickness of sea ice *vis-a-vis* growth and ice strength.

In the remainder of this section, the detailed model equations and numerical scheme are presented. Since the essential features have already been outlined, readers less interested in such details might wish to skip to the simulation results in Section 3.

b. *Model equations*

The equations for the various components of this ice model are presented below.

1) MOMENTUM BALANCE

For the momentum balance the ice is considered to move in a two-dimensional plane with forcing fields operating on the ice via simple planetary boundary layers. In Cartesian coordinates in the plane of motion of the sea ice the momentum balance is

$$m D\mathbf{u}/Dt = -mf\mathbf{k} \times \mathbf{u} + \boldsymbol{\tau}_a + \boldsymbol{\tau}_w - mg\,\mathrm{grad}H + \mathbf{F}, \quad (1)$$

where $D/Dt = \partial/\partial t + \mathbf{u}\cdot\nabla$ is the substantial time derivative, $\mathbf{k}$ a unit vector normal to the surface, $\mathbf{u}$ the ice velocity, f the Coriolis parameter, m the ice mass per unit area, $\boldsymbol{\tau}_a$ and $\boldsymbol{\tau}_w$ forces due to air and water stresses, H the sea surface dynamic height, g the acceleration due to gravity and $\mathbf{F}$ the force due to variation in internal ice stress.

The air and water stress terms in the momentum balance are determined from simple nonlinear integral boundary-layer theories, assuming constant turning angles (Brown, 1979; McPhee, 1975):

$$\boldsymbol{\tau}_a = \rho_a C_a |\mathbf{U}_g| (\mathbf{U}_g \cos\phi + \mathbf{k} \times \mathbf{U}_g \sin\phi), \quad (2)$$

$$\boldsymbol{\tau}_w = \rho_w C_w |\mathbf{U}_w - \mathbf{u}| [(\mathbf{U}_w - \mathbf{u}) \cos\theta + \mathbf{k} \times (\mathbf{U}_w - \mathbf{u}) \sin\theta], \quad (3)$$

where $\mathbf{U}_g$ is the geostrophic wind, $\mathbf{U}_w$ the geostrophic ocean current, C_a and C_w air and water drag coefficients, ρ_a and ρ_w air and water densities and ϕ and θ air and water turning angles. The geostrophic ocean currents are computed by $\mathbf{U}_w = gf^{-1}\mathbf{k} \times \mathrm{grad}H$.

In the atmospheric case the simple integral approach in Eq. (2) consists of estimating the surface wind from the geostrophic wind and then using a square drag law. (In this equation the ice motion has been neglected since the velocity of the air is much larger than the ice velocity.) For the ocean case, the ice velocity relative to the currents beneath the boundary layer is used to estimate a quadratic water drag. In the case that $\mathbf{U}_w$ is neglected the sea ice is effectively considered to be moving across a stagnant ocean with a boundary layer induced by the ice motion. While simple, these integral formulations do appear to give adequate wind and water stress estimates for the ice drift, and have, for example, been used successfully to model stress-free ice drift during the summer (McPhee, 1979).

In all the calculations done here the geostrophic currents are considered to be steady. Estimates of these currents were obtained using long-term values for the sea surface height (Coachman and Aagaard, 1974). While a first step adequate for this study, this approximation ignores some important feedback effects. The stress transmitted into the Arctic Ocean is in large part due to the motion of the ice cover. Consequently, the ice drift (and thus the ice interaction) can modify the ocean currents over a long time period. In light of this fact an important extension of this work would be to couple the ice model to a three-dimensional ocean model for an Arctic Ocean study. Such a study could be compared to Semtner's (1976b) simulations where variable ice interaction effects were not considered.

Arctic observational studies, together with empirical model calculations, have yielded magnitude estimates for the various terms in the momentum balance. Measurements (Thorndike, 1973) indi-

cate that in winter the acceleration term is generally negligible. Between the steady current and wind, the wind stress is the most predominant driving force. Empirical linear calculations (Hibler and Tucker, 1979) show the effects of the steady geostrophic currents and ocean tilt to typically affect ice velocities by only a few percent. However, for cumulative drift over an annual cycle the steady current effects are significant and may account for ~25% of the drift. For locations far from shore, the internal ice stress is normally substantial (e.g., Hunkins, 1975) except over a several-month-long period during the summer (McPhee, 1979; Hibler and Tucker, 1979). However, at nearshore locations it is expected that ice stresses may fluctuate both in winter and summer.

2) CONSTITUTIVE LAW

For modeling the ice interaction the ice is considered to be a nonlinear viscous compressible fluid obeying the constitutive law

$$\sigma_{ij} = 2\eta(\dot{\epsilon}_{ij},P)\dot{\epsilon}_{ij} + [\zeta(\dot{\epsilon}_{ij},P) - \eta(\dot{\epsilon}_{ij},P)]\dot{\epsilon}_{kk}\delta_{ij} - P\delta_{ij}/2, \quad (4)$$

where σ_{ij} is the two-dimensional stress tensor, $\dot{\epsilon}_{ij}$ the strain rate tensor, $P/2$ a pressure term (taken to be a function of the ice thickness characteristics as discussed later), and ζ and η nonlinear bulk and shear viscosities. Using this constitutive law the force components due to internal ice stress (calculated from $F_i = \partial\sigma_{ij}/\partial x_j$) are

$$F_x = (\partial/\partial x)\{[\eta + \zeta]\partial u/\partial x + [\zeta - \eta]\partial v/\partial y - P/2\} + (\partial/\partial y)[\eta(\partial u/\partial y + \partial v/\partial x)], \quad (5)$$

$$F_y = (\partial/\partial y)\{[\eta + \zeta]\partial v/\partial y + [\zeta - \eta]\partial u/\partial x - P/2\} + (\partial/\partial x)[\eta(\partial u/\partial y + \partial v/\partial x)]. \quad (6)$$

For calculations performed here the dependence of ζ and η on $\dot{\epsilon}_{ij}$ and P is normally taken so that the stress state lies on an elliptical yield curve passing through the origin (see Fig. 2) with a no-stress condition applying for pure divergence:

$$\zeta = P/2\Delta, \quad (7)$$

$$\eta = \zeta/e^2, \quad (8)$$

$$\Delta = [(\dot{\epsilon}_{11}^2 + \dot{\epsilon}_{22}^2)(1 + 1/e^2) + 4e^{-2}\dot{\epsilon}_{12}^2 + 2\dot{\epsilon}_{11}\dot{\epsilon}_{22}(1 - 1/e^2)]^{1/2}, \quad (9)$$

where e is the ratio of principal axes of the ellipse. [A derivation of this equation assuming rigid plastic flow, together with a normal flow rule, is given in Hibler (1977).] For very small strain rates the viscosities in Eqs. (7) and (8) become arbitrarily large. To avoid this they are chosen to be the minimum of the plastic values [Eqs. (7) and (8)] and some large limiting values dependent on the ice strength P. When this occurs the stress state lies on some concentric ellipse inside the yield surface such as the dashed example in Fig. 2. In practice these limiting values are chosen to be large enough to be rarely reached so that they do not significantly affect the computations. For the calculations performed here the limiting values were taken to be

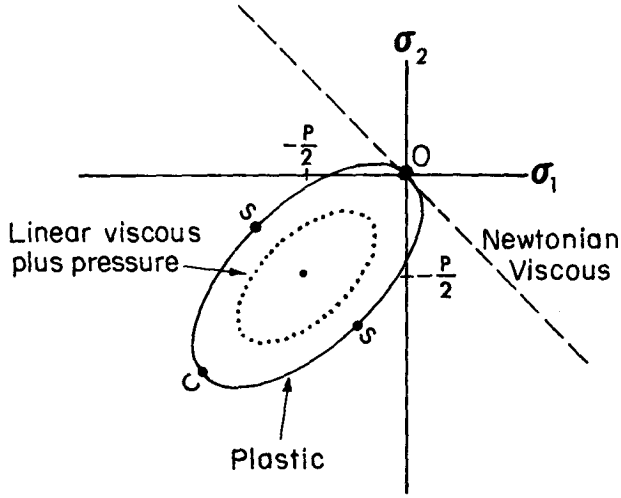

FIG. 2. Relationship between the principal components of stress (σ_1 and σ_2) for a viscous-plastic rheology employing an elliptical yield curve with a principal axes ratio e of 2. For plastic flow, the stress state lies on the solid curve with the location dictated by the ratio of the strain rate principal components. For example, the stress state for pure shearing deformation is located at S, and at C for isotropic compression. For very small strain rates the stress state moves inside the yield curve as illustrated by the dotted curve. For comparison, the stress states for a Newtonian viscous fluid lie on the dashed line. In all cases negative values of σ_1 and σ_2 represent compressive stresses and positive values tensile stresses.

$$\zeta_{max} = (2.5 \times 10^8 \text{ s})P, \quad (10)$$

$$\eta_{max} = \zeta_{max}/e^2, \quad (11)$$

and in practice are reached only for deformation rates $\lesssim 10^{-4}$ day^{-1}.

For comparison, Fig. 2 also shows the stress state for a Newtonian viscous fluid as used, for example, by Campbell (1965). For the Newtonian viscous fluid the constitutive law is given by

$$\sigma_{ij} = 2\eta[\dot{\epsilon}_{ij} - 0.5\dot{\epsilon}_{kk}\delta_{ij}]. \quad (12)$$

This simple rheology has been used by a number of authors (e.g., Kulakov *et al.*, 1979; Doronin, 1970) and has the advantage of being similar to viscosity parameterizations used in ocean models. However, its physical basis for use in sea ice modeling is questionable.

The choice of the particular plastic constitutive law specified by Eqs. (4)–(9) does have some

physical motivation. In particular this choice is based on the following assumptions, deemed reasonable for sea ice: (i) on a reasonably large-scale sea ice is on the average isotropic; (ii) the effective tensile strength is invariably low, regardless of the kind of deformation; (iii) stresses are relatively independent of strain rate magnitude (the plastic hypothesis); and (iv) sea ice has substantial compressive strength under convergence. Much of the justification for the important plastic assumption is based on physical arguments that the work done in deformation is relatively rate independent (e.g., see Coon, 1979). The elliptical yield curve satisfies these characteristics and has the additional attraction of computational simplicity. More complicated yield curves, such as the tear-drop shape suggested by Rothrock (1975b), could be included here, if desired, by allowing a more complex dependence of η and ζ on P and $\dot{\epsilon}_{ij}$.

Note that as is normal in compressible fluids, the pressure term in (4) is distinguished from the compression term containing the bulk viscosity (which also contributes to the trace of the stress tensor) by the fact that it is independent of strain rate. This fact, together with the closure scheme (limiting the viscosities to some maximum value), forms the essential difference between this viscous-plastic approach and the conventional elastic-plastic approach (Goodier and Hodge, 1958).

3) Ice thickness characteristics

Typically, a sea ice cover will contain a variety of ice thicknesses. Because of this variable thickness feature, appreciable fractions of both thin and thick ice can be present at the same time in a given region. For energy exchange purposes, the young (i.e., thin) portion of the ice cover is particularly important. Arctic heat transport studies, for example (Maykut, 1978), indicate that winter heat input into the atmosphere from ice in the 0–0.4 m range can be one to two orders of magnitude larger than from the thicker perennial ice. In practice, the fraction of thin ice is affected by both deformation and thermodynamics. Deformation can create thin ice by divergence and remove thin ice by convergence. Growth will diminish the amount of thin ice by converting it into thicker ice, whereas melt can create thin ice and/or open water by gradually reducing the ice thickness.

To approximately parameterize this variable thickness ice cover, two idealized thickness levels are used in this model: thick and thin. To keep track of these two levels, two quantities are calculated—the mass of ice in any grid cell (in the form of an equivalent ice thickness h) and the compactness A, which is defined as the fraction of the grid cell area covered by thick ice. The rest of the cell is covered by thin ice which, for computational convenience, is always taken to be of zero thickness (i.e., open water). The idea here is to have the open water approximately represent the combined fraction of both open water and thin ice up to some cutoff thickness h_0. The remainder of the ice is distributed arbitrarily. However, since the thin ice mass is normally small, the mean thickness of the remaining "thick" ice is approximately equal to h/A.

For the mean thickness h and compactness A the following continuity equations are used:

$$\partial h/\partial t = -\partial(uh)/\partial x - \partial(vh)/\partial y + S_h + \text{diffusion}, \quad (13)$$

$$\partial A/\partial t = -\partial(uA)/\partial x - \partial(vA)/\partial y + S_A + \text{diffusion}, \quad (14)$$

where $A \leq 1$ and S_h and S_A are thermodynamic terms given by

$$S_h = f(h/A)A + (1 - A)f(0), \quad (15)$$

$$S_A = \begin{cases} (f(0)/h_0)(1 - A), & \text{if } f(0) > 0, \\ 0, & \text{if } f(0) < 0, \end{cases} + \begin{cases} 0, & \text{if } S_h > 0, \\ (A/2h)S_h & \text{if } S_h < 0, \end{cases} \quad (16)$$

with $f(h)$ the growth rate of ice of thickness h, and h_0 a fixed demarcation thickness between thin and thick ice (0.5 m is used here for the standard simulation). The diffusion terms, which are small, have been added for numerical stability. While (13) is a simple continuity equation for the ice mass (characterized by the mean thickness h), with thermodynamic source and sink terms, Eq. (14) is somewhat more complex. By including the restriction that $A \leq 1$, a mechanical sink term for the areal fraction of ice has been added to a simple continuity equation for the ice concentration. This sink term turns on when $A = 1$ (i.e., no open water left) and under converging conditions removes enough ice area through ridging to prevent further increase in A. Although the sink term does not change the ice mass, it can cause the "thick" ice thickness to increase by allowing h to increase while A does not. A more formal derivation of the dynamic portion of Eq. (14) is given by Thorndike *et al.* (1975) in which more general mechanical source and sink terms are also considered.

The effects of growth and decay on the thickness distribution are represented by the terms S_h and S_A. The net ice growth or melt is given by S_h. Within the two-level approximation, S_h is given by the sum of the ice grown on open water plus the additional growth over the portion of the cell covered by thick ice. To approximate the growth and decay rate of this thick ice, its mean growth

rate is estimated to be that of ice of constant thickness h/A. For melting conditions the same sum over open water and thick ice is used. The assumption here is that the heat absorbed by open water will horizontally mix and melt additional ice until the mixed layer returns to freezing. Overall, the ice growth and decay simulated by the S_A term qualitatively approximates the relative thermodynamic roles of thin and thick ice. However, due to the lack of thickness detail, quantitative differences will occur.

The S_A term characterizes the way in which growth and decay change the relative areal extents of thin and thick ice. The basic physical notion embodied by this term is that the areal fraction of thin ice will decrease rapidly under freezing conditions, and increase slowly under melting conditions. To simply parameterize the freezing effect, the fraction of open water $(1 - A)$ is allowed to decay exponentially with a time constant of $h_0/f(0)$, which gives the first term in Eq. (16). In practice, h_0 is chosen to be small compared to mean ice thicknesses but large enough so that heat fluxes through h_0-thick ice are substantially less than through open water. For the standard simulation $h_0 = 0.5$ m is used. Under winter growth conditions this value will yield decay times of ~5 days. A less obvious secondary effect, arising from the removal of thin ice by freezing, is a decrease in the mean thick ice thickness h/A. This occurs because A increases faster than h under growth conditions. Such an effect is desirable since in reality the mean thickness of the "thick" ice becomes smaller as the thin ice is added.

The second term in (16) accounts for melting. Its magnitude is derived by assuming that the thick ice is uniformly distributed between 0 and $2\,h/A$ in thickness, and all melts at the same rate. Therefore, over a time Δt the ice of thickness less than $S_h\,\Delta t$ will melt and form open water. By the assumption of uniform distribution this ice covers a fraction of area equal to $S_h\,\Delta t\,A/2h$, which for Δt small yields the second term in the equation for S_A. It should be noted that this melting term also nonphysically creates small amounts of open water due to ablation of very thick ice in winter. However, the magnitude of this effect is essentially negligible.

In practice the freezing term in (16) is fairly important in the calculations since it affects the important fraction of thin ice in winter. The melting term is of less importance and accounts for only a few percent of the open water formed in summer. For comparison, simulations are also made in this paper with only one layer of ice used (i.e., $A = 1$ identically).

A key component of both the thermodynamic terms S_h and S_A is the growth rate function $f(h)$.

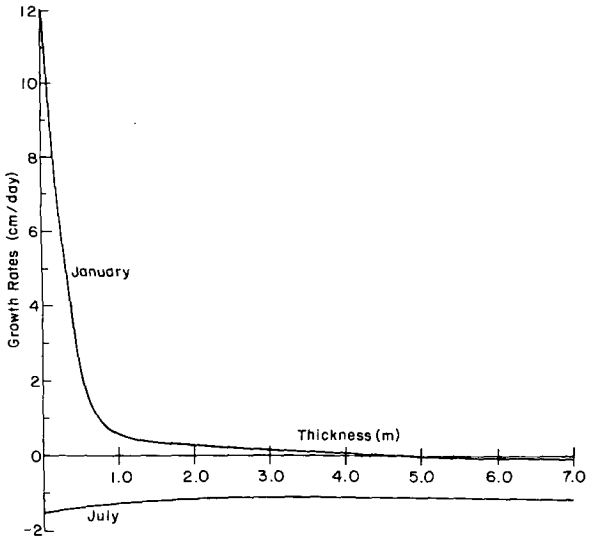

FIG. 3. Typical growth rates of sea ice used for seasonal simulations.

To calculate $f(h)$ properly a complete heat budget should be done at each timestep separately over open water and ice; however, to simplify sensitivity studies, seasonal growth rates estimated by Thorndike *et al.* (1975) for the central basin were used everywhere in the Arctic Ocean. Typical growth rates versus thickness for winter and summer conditions are shown in Fig. 3. These growth rates were partially based on heat budget calculations by Maykut and Untersteiner (1971) which include an oceanic heat flux from below the mixed layer. This parameterization supplies a reasonable facsimile of a complete heat budget at each step, without, of course, geographical variations or feedback effects in the boundary layers. However, it is certainly clear that the inclusion of a proper heat budget in a simulation model of this type is essential in more complete studies, and is an important extension to this work.

It is notable in Eq. (16) that the rate of removal of thin ice under growth is independent of the thick ice thickness. The basic idea here is to incorporate the thin ice into the thick portion of the ice cover once its growth rate has been substantially reduced. Besides being physically reasonable, this feature also aids in the interpretation of the simulation results. It should be noted that this procedure differs from the approach used by Parkinson and Washington (1979) in conjunction with climatologically averaged input data. There, the heat lost through a lead is used to accumulate ice onto the side of the thick ice. Within the formulation of (16) the net effect of the Parkinson and Washington parameterization is to change h_0 to h/A, which will be generally much larger than h_0. Hence, under growth, thin ice disappears more slowly than in

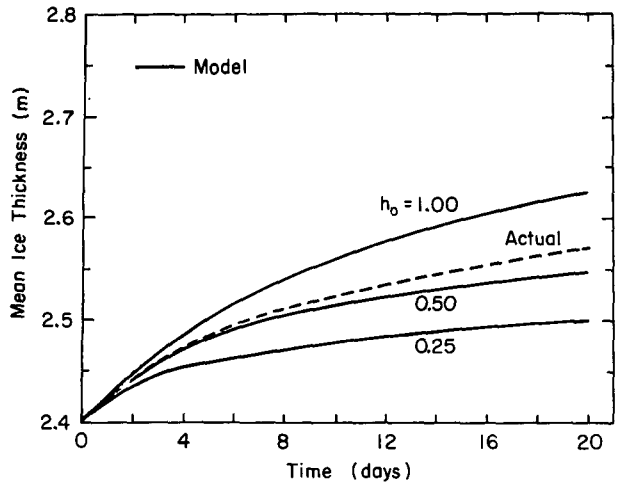

FIG. 4. Simulated and actual ice growth using different thin ice parameterizations. Initial conditions were 20% open water and 80% coverage by 3 m thick ice. In the actual ice growth case the thin ice reaches a 0.5 m thickness in slightly less than 9 days.

reality. While such a feature may well be desirable for climatologically averaged forcing fields, it makes interpretation of the effects of deformation on ice growth rather difficult.

The utility of Eqs. (15) and (16) and the importance of the h_0 parameter are perhaps best illustrated by results from a simple thermodynamic experiment, shown in Fig. 4. Here, mean simulated ice thicknesses versus time are compared to the actual thickness. In all cases January growth rates were used together with initial conditions of 20% open water and 80% of 3 m thick ice. As can be seen, the choice of $h_0 = 0.5$, which is used in the standard simulation, is reasonable. With larger values of h_0, on the other hand, the thin ice growth tends to be overestimated.

With respect to the diffusion, small harmonic and biharmonic diffusion terms have been added for stabilization over long-term integrations, e.g., $(\text{diffusion})_h = D_1\nabla^2 h + D_2\nabla^4 h$. Of these two terms the biharmonic diffusion is most important, and is taken to be four times as large as the harmonic diffusion at the Nyquist wavenumber. Although in practice there may be some actual diffusion in the sea ice due to random effects, the diffusion used here is viewed primarily as a necessary numerical artifact to suppress smaller scales in order to avoid aliasing. The diffusion is dependent on the grid size and is smaller for finer grids.

4) THICKNESS-DYNAMIC COUPLING

To couple the ice strength to the ice thickness characteristics the ice pressure $P/2$ (and hence indirectly the viscosities) is taken to be a function of compactness and thickness according to

$$P = P^* h \exp[-C(1 - A)], \qquad (17)$$

where P^* and C are fixed empirical constants and h is in meters. This formulation makes the strength strongly dependent on the amount of thin ice (characterized by the compactness A), while also allowing the ice to strengthen as it becomes thicker. Within the framework of the compressible fluid approach used here, this relation effectively forms an equation of state for the pressure, which is necessary to complete the system of equations. In this equation of state no temperature or salinity dependence is included since such variables are felt to have only a second-order effect on the strength of the ice interaction.

While directly intuitive, the strength expression in (17) can also be qualitatively related to the strength assumptions used in the multilevel thickness distribution of Thorndike *et al.* (1975). There, following a suggestion by Rothrock (1975b), the strength of the ice is explicitly related to the work done by ridging. Under converging conditions, the closure of both thin and thick ice (and also open water) occurs simultaneously. The relative amount of thin ice being deformed, however, is weighted by the area of thin ice. Hence for small amounts of thin ice, more thick ice is deformed and thus the ice has a high strength which is dependent on the thick ice characteristics. For a large amount of thin ice, on the other hand, mostly thin ice is deformed which yields low strength. These features are represented in Eq. (17) by the exponential dependence on $(1\text{-}A)$ which characterizes the amount of thin ice being ridged, and the proportionality to h which approximates the strength of thick ice undergoing deformation. The assumption in the h dependence is that the distribution of thick ice is reasonably well described by its mean (h/A). However, while qualitatively correct, this two-level ice thickness scheme does not allow the particular thickness of ice involved in ridging to be determined.

c. *Numerical scheme*

The simultaneous equations (1), (13), (14) and (17) are numerically solved as an initial-value problem using finite-difference techniques. A staggered, spatial grid configuration similar to that employed in ocean models (Bryan, 1969) is used (Fig. 5). This configuration allows the continuity equations to be cast in mass-conserving form and in energy-conserving form for the incompressible components of the velocity field. Also, the viscous terms can be formulated in energy-conserving form in the momentum equations. For completeness the finite-difference code for the momentum equations (together with the relaxation scheme) and the continuity equations is outlined in Appendix A.

For solution of the momentum equations [Eq. (1)] a semi-implicit predictor corrector procedure (Ames, 1969) is used to center the nonlinear terms. Under this procedure two relaxation solutions are required at each timestep, one to center the nonlinear terms and one to advance to the next step. In each case point relaxation techniques are used to solve the linearized implicit equations. The acceleration term is included by a backward time step, although its contribution is effectively negligible for timesteps longer than several hours (see Appendix B). This backward timestep does overdamp the inertial oscillations, but at timesteps used here (1 day) such terms are not considered important. Also, the Coriolis terms can easily be made neutrally stable by considering them separately if desired.

The ice thickness equations (13) and (14) are integrated explicitly, with the advection terms integrated by a modified Euler step (Kurihara, 1965)—which is second-order accurate in time—and the diffusion and thermodynamic terms by a forward Euler step. The diffusion terms render the system linearly stable in addition to preventing the buildup of nonlinear instabilities. In practice these diffusive terms make only small contributions, and in the standard simulation discussed next the diffusive fluxes were less than 3% of the advective fluxes on the average.

This time-marching procedure for the coupled equations can be conveniently illustrated using the simplified one-dimensional equations:

$$\partial u/\partial t = (\partial/\partial x)[\eta(u,P)\partial u/\partial x] - D(u)u - \partial P/\partial x - u(\partial u/\partial x), \quad (18)$$

$$\partial h/\partial t = -\partial(uh)/\partial x + f(h) - Dh, \quad (19)$$

$$P = P(h), \quad (20)$$

where, for illustrative purposes, the diffusion term has been replaced by a simple drag term. In time, h is considered to be defined at $t^{i+1/2}$ and u at t^i. To advance u requires two steps (denoting spatial differences by δ_x and time location by superscripts):

$$u^{i+1/2} = u^i + \tfrac{1}{2}\Delta t\{\delta_x[\eta(u^i,P^{i+1/2})\delta_x u^{i+1/2}] - D(u^i)u^{i+1/2} - \delta_x P^{i+1/2} - u^i\delta_x u^{i+1/2}\}, \quad (21)$$

$$u^{i+1} = u^i + \Delta t\{\delta_x[\eta(u^{i+1/2},P^{i+1/2})\delta_x u^{i+1}] - D(u^{i+1/2})u^{i+1} - \delta_x P^{i+1/2} - u^{i+1/2}\delta_x u^{i+1}\}, \quad (22)$$

where both equations are solved for the u's by relaxation. Note that Eq. (21) provides an estimate of $u^{i+1/2}$ for use in the nonlinear terms in the basic timestep [Eq. (22)]. Once the velocity has been advanced to time t^{i+1} the thickness is then advanced by the two-step procedure, i.e.,

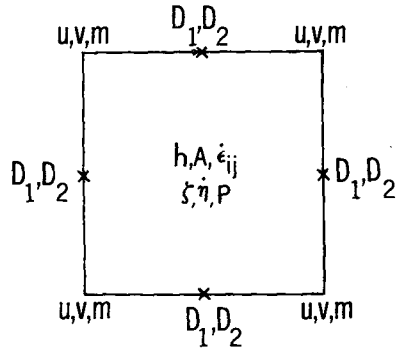

FIG. 5. Spatial arrangement of variables used in numerical calculations.

$$h^{i+3/2*} = h^{i+1/2} - \Delta t\delta_x(u^{i+1},h^{i+1/2}), \quad (23)$$

$$h^{i+3/2} = h^{i+1/2} - \Delta t\{\delta_x[u^{i+1}(h^{i+1/2} + h^{i+3/2*})/2] - Dh^{i+1/2} + f(h^{i+1/2})\}. \quad (24)$$

The first equation in this modified Euler procedure provides a provisional value in order to approximately center the advection term in the second equation. Note that since h and u are staggered in time the coupled system is effectively being integrated by the efficient forward–backward scheme (Mesinger and Arakawa, 1976).

The essential stability requirement on the system of equations is a Courant-Friedrichs-Lewy condition for the advection terms: $\Delta t \leq \Delta x[2(u^2 + v^2)]^{-1/2}$. In addition, in order to insure against any nonlinear instabilities, the viscosity parameter is never allowed to drop below $\zeta = 4.0 \times 10^8$ kg s^{-1}. This value is several orders of magnitude below typical strong ice interaction values and effectively yields free drift results. There is also, in principle, the possibility of a gravity wave due to the coupling of the pressure with acceleration. However, a local stability analysis indicates that the large ice viscosities, related to the pressure, keep the system stable for backward timesteps of any magnitude.

Although not a formal stability requirement, it is also wise to choose timesteps small compared to the scale of variability of the forcing. This is because the nonlinear viscosity takes a few time steps to adjust to changes in the forcing field due to the semi-implicit treatment of the nonlinear terms. Results for a constant-forcing field, reported in Appendix B, show this response time to be about four or five timesteps if large timestep magnitudes (~1 day) are used in the integration. Results in Appendix B also verify that the momentum equilibrium state for fixed forcing is independent of the timestep magnitude used in the integration.

3. Simulation results

To examine the characteristics and usefulness of this model a number of numerical experiments were

carried out. The approach in these experiments was to use observed time-varying wind data to drive the model over time periods long enough to obtain seasonally varying equilibrium results. (Certain more idealized test simulations are discussed in Appendices B and C.) For the primary experiment the model was applied to the Arctic Basin and integrated for eight years (using observed time-varying wind data) at 1-day timesteps and a resolution of 125 km in order to obtain results essentially independent of initial conditions. The results are compared with various observed data, including ice drift, geographical and temporal ice thickness variations, ice ridge statistics, ice concentration charts and mass balance statistics. A rectangular grid (Fig. 6), based on a stereographic projection, was used in the simulations. The Coriolis parameter was taken to be constant over the whole grid. This f-plane approximation was felt to be adequate for this study because of the slow variation of the Coriolis parameter in the polar regions and has been commonly used in studies of Arctic ice drift (e.g., Rothrock, 1975a). The numbered grid cells and circled grid points denote locations used for time series results. To obtain a natural outflow condition the ice thickness (for estimating strength) was taken to be zero in the shaded grid cells between Spitsbergen and Greenland. Average thickness and compactness values based on neighboring grid cell values, however, were used in the continuity equations to preserve second-order accuracy.

For input wind data to drive the simulations, observed surface pressure data over the time period May 1962–May 1963 were used to construct 8-day averaged geostrophic winds. The wind data were then modified in the May portion of the record to create a one-year periodic result. (This particular time interval was used because of the simultaneous presence of one U.S.S.R. and two U.S. drifting ice stations, which provided observed ice velocity and deformation rate information.) The pressure data were obtained from the National Center for Atmospheric Research and were reported every other 5° of latitude and longitude. These data were converted to a 16 by 16, 250 km square mesh grid (containing the Arctic Basin grid in Fig. 6) using the cubic spline gridding procedure discussed by Davis and Kontis (1970). The data were then smoothed and differentiated using discrete Fourier transforms and interpolations made to the finer mesh Arctic Basin grid. For the calculation of geostrophic currents, mean dynamic topography values reported by Coachman and Aagaard (1974) were used. Thermodynamic growth rates (no geographical variation) as a function of thickness and time were taken from Thorndike *et al.* (1975). Table 1 gives the numerical parameters used in this standard simulation.

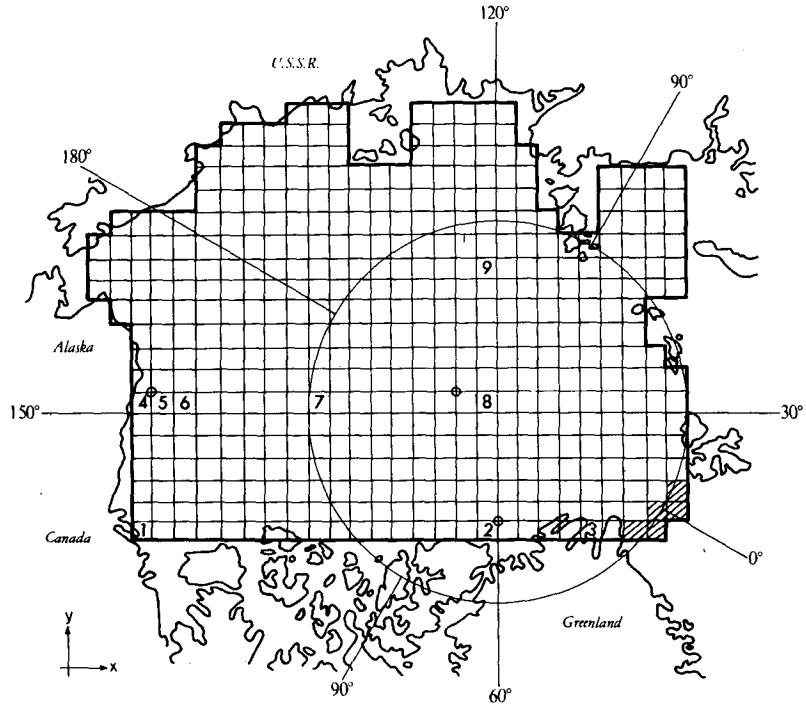

FIG. 6. Fixed square-mesh grid used for numerical calculations. The numbered grid cells and circled grid points denote locations of time series plots of ice characteristics.

It should be noted that besides the wind and water drag coefficients the key constants are P^*, e, h_0 and C. The constants P^* and C relate the ice strength to the ice thickness and compactness [Eq. (17)], e is the principal axes ratio of the plastic yield curve [Eqs. (8) and (9)], and h_0 determines the rate of decay of the fraction of open water due to growth [Eq. (16)]. Viscous studies (Hibler, 1974) suggest η to be smaller than ζ, so $e = 2$ (which yields a ζ/η ratio of 4) is reasonable. C is determined so that 10% open water reduces the strength substantially. h_0 was chosen to give a typical winter time scale of about 5 days for the removal of open water through growth (see Fig. 4). The wind and water drag coefficients and turning angles were taken from McPhee (1979). P^* is the basic, free empirical parameter and was adjusted to give reasonable agreement between the predicted and observed net drift of the drifting stations over this year-long period. The P^* value found to be useful in the standard simulation is slightly larger than, although of the same order of magnitude as, values estimated by Thorndike *et al.* (1975). Sensitivity of the simulation results to these parameters is discussed later in this section. Initial conditions in all cases were taken to be a constant ice thickness of 3.2967 m ($=3.0 \times 10^3$ kg m$^{-2}/\rho_I$) and a compactness of 1.0 on Julian Day 1.

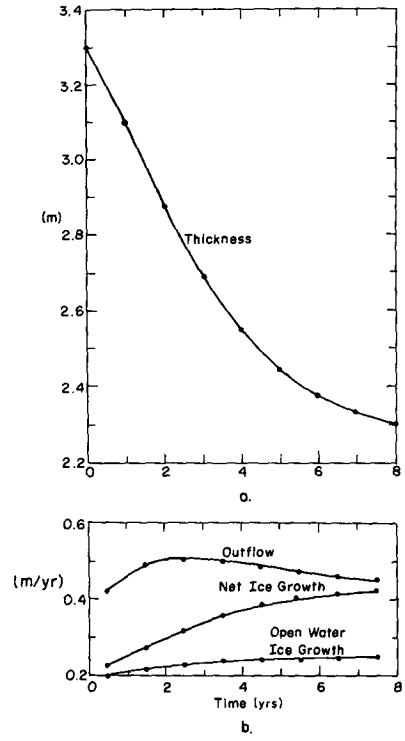

FIG. 7. Average basin ice thickness versus time for the standard simulation (a), and the annual average ice outflow, net growth and net growth over open water (b).

a. Equilibrium time scales

After several years of integration the model approaches a cyclic equilibrium, with thickness and velocity characteristics taking on similar values on corresponding days of successive years. Fig. 7 shows the basin-averaged mean ice thickness on 1 January of successive years. Also shown in this figure are the averaged annual net growth, outflow and net growth over open water. Initially the net ice growth is substantially less than the flow out of the basin. However, as the ice becomes thinner the growth increases until after eight years it almost balances the outflow. The figure also shows that due to the initially thick ice, the growth early in the simulation is dominated by the ice formation over open water. As the ice becomes thinner, however, the ice growth over ice-covered portions of the basin becomes more significant. At the end of the eighth year the system is very close to equilibrium, with a mean thickness decrease of less than 3 cm from the previous year. Fitting an exponential to the thickness change versus time shows the time scale for thickness equilibrium to be ~2.5 years. Such a time scale is reasonable since the total equilibrium is basically thermodynamic in nature, with the slow growth effects gradually catching up to the outflow.

TABLE 1. Numerical parameters used in standard simulation.

$C_a = 0.0012$	$\Delta x = \Delta y = 125$ km
$C_W = 0.0055$	$\Delta t = 1$ day
$C = 20.0$	$\zeta_{max} = (P/4) \times 10^9$ kg s^{-1}
$e = 2$	$\eta_{max} = \zeta_{max}/e^2$
$f = 1.46 \times 10^{-4}$ s^{-1}	$\rho_I = 0.91 \times 10^3$ kg m^{-3}
$h_0 = 0.5$ m	$\phi = \theta = 25°$
$\rho_a = 1.3$ kg m^{-3}	$D_1 = 0.004\Delta x = 5.0 \times 10^2$ m^2 s^{-1}
$P^* = 5.0 \times 10^3$ N m^{-1}	$D_2 = \Delta x^2 D_1 = 7.81 \times 10^{12}$ m^4 s^{-1}

The time scale for the change of velocity due to ice buildup (and hence strengthening) of nearshore ice is somewhat faster. For example, Fig. 8 shows the x and y ice velocity components at grid cell 2 along the Canadian Archipelago where the ice buildup is substantial. After one year the velocity has changed substantially and the general nature of the difference of the equilibrium state from the initial conditions can be determined. In Fig. 8 the initial change in velocity is due to the ice buildup, with the slow decay reflecting the overall slow decrease in basin ice thickness. Simple tests with constant wind fields (an example is given in Appendix C) indicate that this buildup of ice and the subsequent velocity change can in fact take place in only a few weeks. Both these time scales, however, are in contrast to the time scale for the ice velocity to come to equilibrium with the wind. This time scale, examined in Appendix B, is of the order of

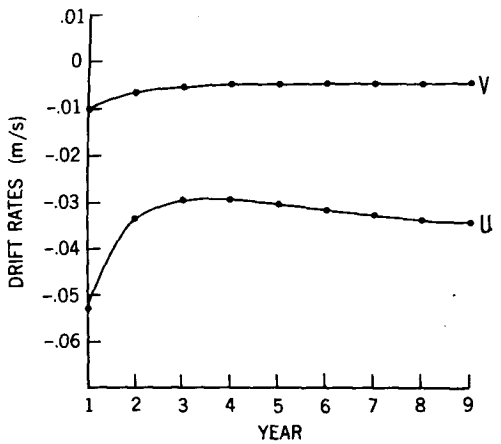

FIG. 8. Drift rates at grid point two on 17 January of successive years in the standard simulation.

hours. Consequently, deformation of the ice pack due to synoptic winds can effectively follow a moving weather system across the basin.

b. Ice velocity characteristics

Fig. 9 shows the average annual ice velocity field for the eighth year of the simulation. This field exhibits many of the characteristics of the average annual ice drift which is outlined, following Gordienko (1958), in Fig. 10. In particular there is a clockwise Beaufort gyre and a transpolar drift stream extending from the Siberian coast to the Greenland-Spitsbergen passage. It is notable that the gyre velocities are substantial even near shore and the ice velocities near the Pole are oriented relatively parallel to the coast. These two particular features can also be produced by assuming the ice to be incompressible (Rothrock, 1975a). However, they are reproduced poorly by free drift estimates (e.g., Felzenbaum, 1958) and Newtonian viscous models (e.g., Campbell, 1965).

It is important to remember that the average circulation, shown in Fig. 9, represents a sum of ice velocities using a complete nonlinear simulation model operating on time-varying wind fields. This can be contrasted to the average circulation estimated by Felzenbaum (1958), Campbell (1965) and Rothrock (1975a) which are obtained using dynamical calculations only, based on a mean annual wind field. Simulated rates averaged over a few days or weeks will usually be larger than the mean annual case and can differ totally in drift pattern. For example, the average January velocity field shown in Fig. 11 has a somewhat similar pattern to the mean annual drift but substantially larger velocities.

Of particular interest in the January velocity field is the strong shearing motion off the Alaskan coast, where the velocity component tangential to the shore is larger near shore than further out due to the plastic rheology allowing a "slip plane" of low viscosity to form. This type of behavior has been

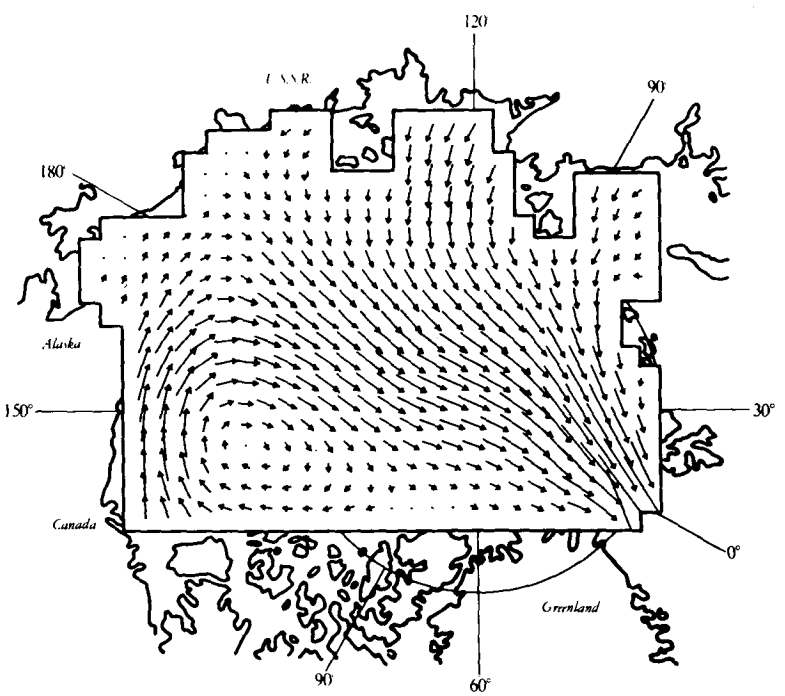

FIG. 9. Average annual ice velocity field for the standard simulation. A velocity vector one grid space long represents 0.02 m s^{-1}.

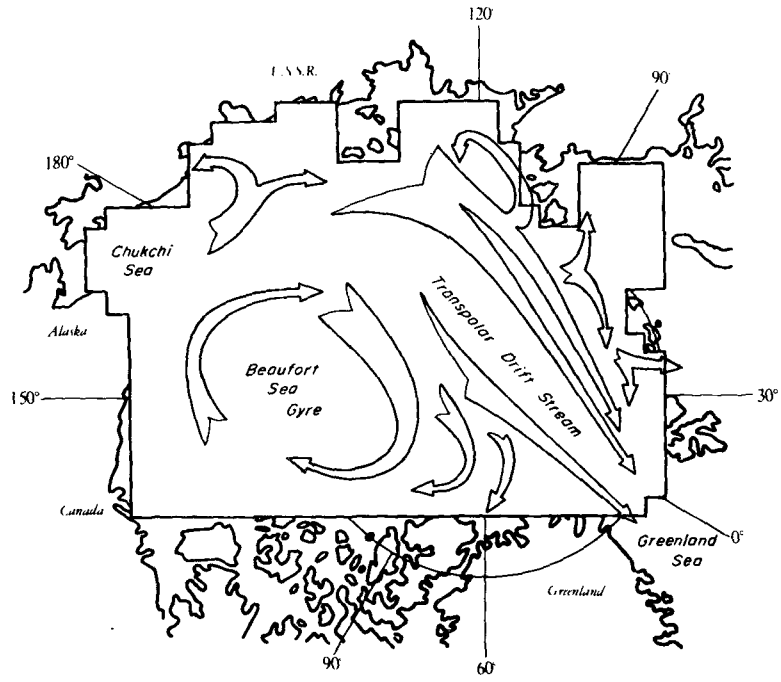

FIG. 10. The pattern of mean drift in the Arctic Ocean (adapted from Gordienko, 1958).

documented observationally using remote sensing imagery by Hibler *et al.* (1974b) and Reimnitz *et al.* (1978).

A more detailed analysis of nearshore ice characteristics more graphically illustrates the formation of such a shear zone off the north coast of Alaska. In Fig. 12 are shown bulk viscosity values for three grid cells progressively further away from the coast together with the nearshore compressive stress (σ_{xx}) and ice velocity. These time series show

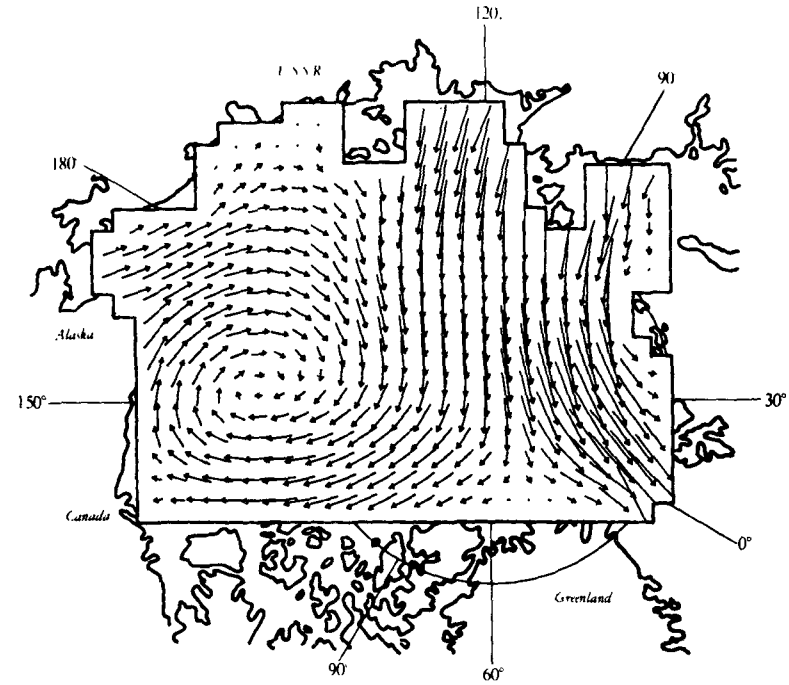

FIG. 11. Average January ice velocity field for the standard simulation. A velocity vector one grid space long represents 0.02 m s^{-1}.

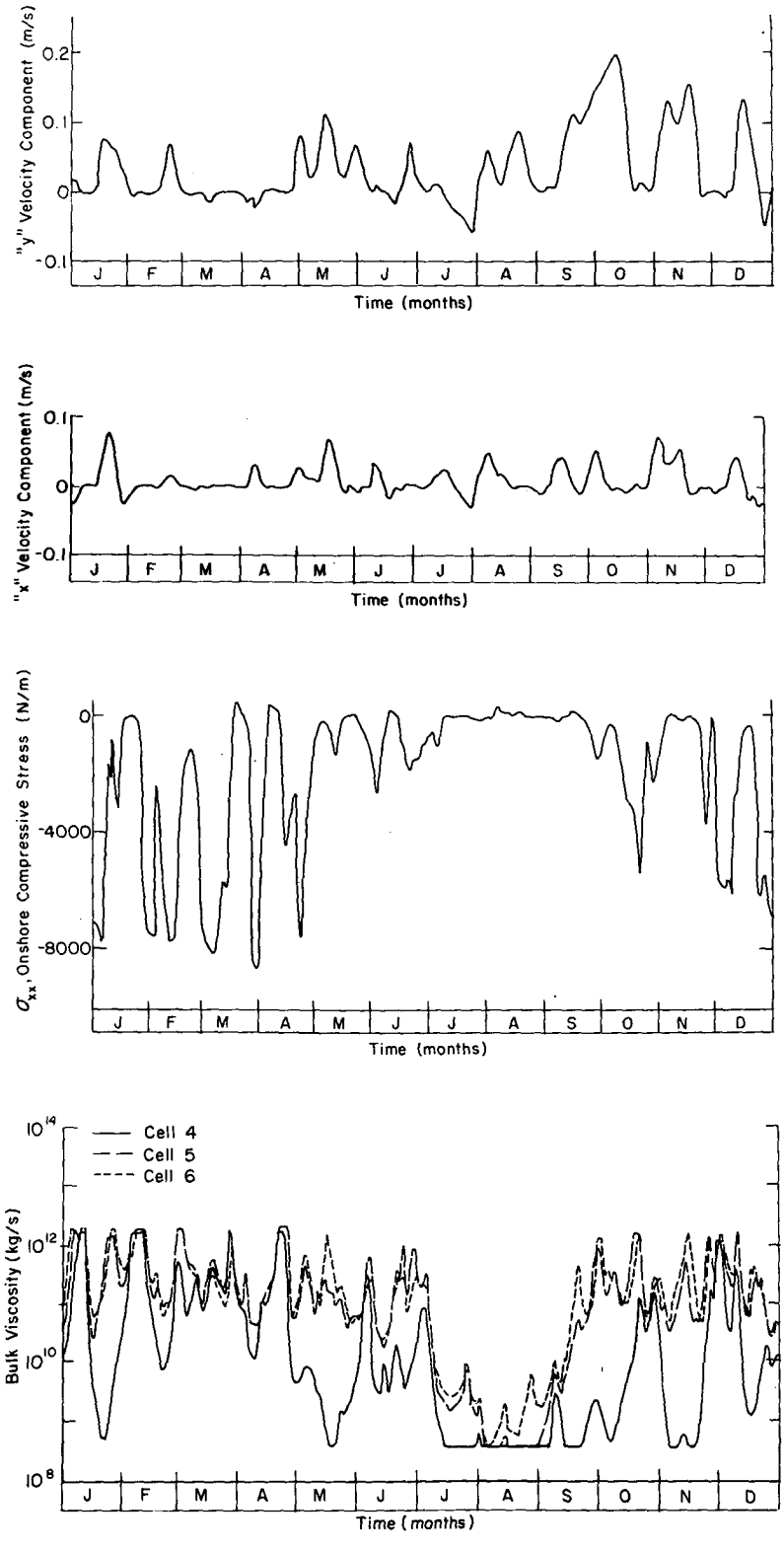

FIG. 12. Nearshore ice characteristics time series illustrating shear zone effects. The bulk viscosities are taken from grid cells progressively further from the coast with the onshore compressive stress and the ice velocities taken from the grid cell and grid point nearest the coast (i.e., grid cell 4 and the circled grid point on cell 4).

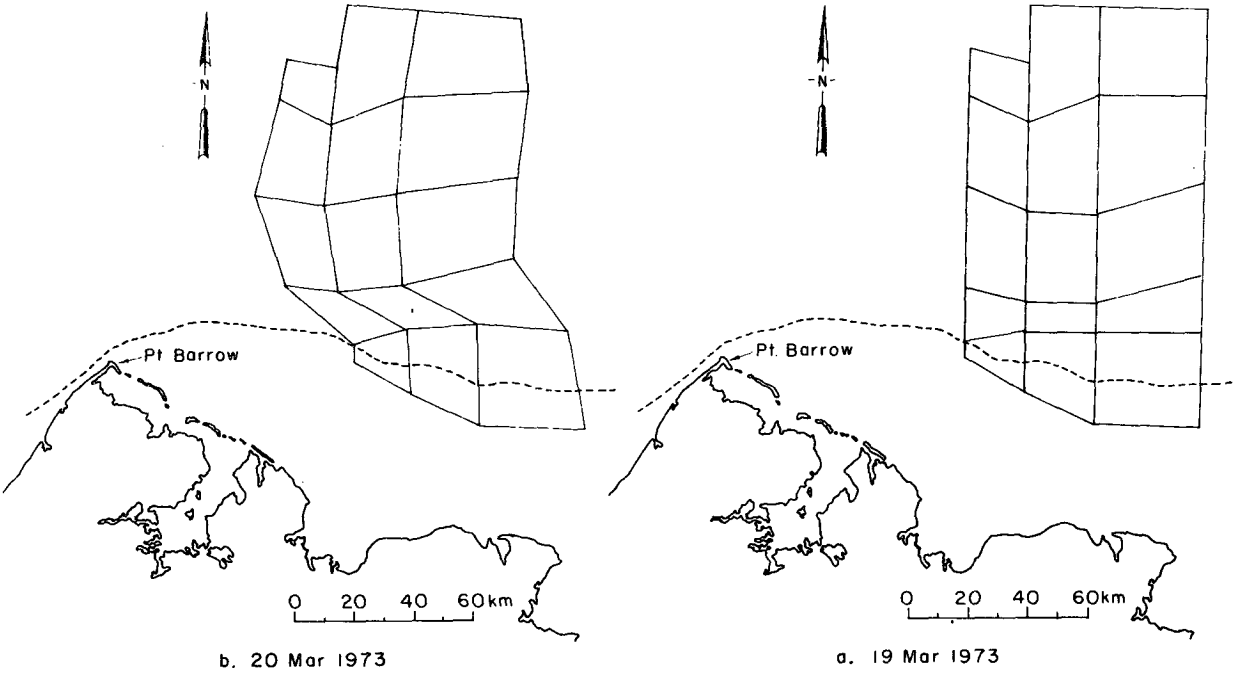

FIG. 13. Observed ice motion pattern over a 1-day interval during shear activity in the nearshore region. The observations were made using LANDSAT imagery and the dashed line marks the boundary between the shore-fast ice and the pack ice.

simulated nearshore deformation events similar to those observed in LANDSAT studies. For example, Fig. 13 shows observed ice motion off Pt. Barrow during a shearing event (Hibler *et al.*, 1974b). The basic characteristic is that as the ice moves out, the nearshore region develops a low viscosity layer, so that the pack can slip along the shear zone in a relatively free manner. This type of behavior is particularly apparent in the spring in the simulation when a large deformation event took place. As is apparent from the figure the reduction of the nearshore viscosity usually coincides with rapid ice motion parallel to the coast (westward) and a decrease in the onshore stress. Under strong onshore stress conditions, on the other hand, relatively little motion takes place.

For a comparison of the simulated drift in the central basin with observations, the simulated velocities of two U.S. and one U.S.S.R. drifting ice stations were estimated by taking the calculated velocity at the grid point nearest the station location on any given day. Fig. 14 shows simulated and observed 11-day smoothed x and y velocity components for one of these stations (ice station *Arlis*). For an estimate of the net ice station displacement, the observed and simulated velocities of all three stations were summed from day 140 (1962) to day 109 (1963). The results are shown in Fig. 15. These drift comparisons show the simulated velocities and cumulative drift to be in good agreement with the observed values, especially considering that errors due to inadequate current data and poorly resolved wind fields can be substantial.

Drift results far from shore, similar to those shown in Figs. 14 and 15, can also be obtained using simpler linear models without ice thickness effects (i.e., Hibler and Tucker, 1979). However, in such

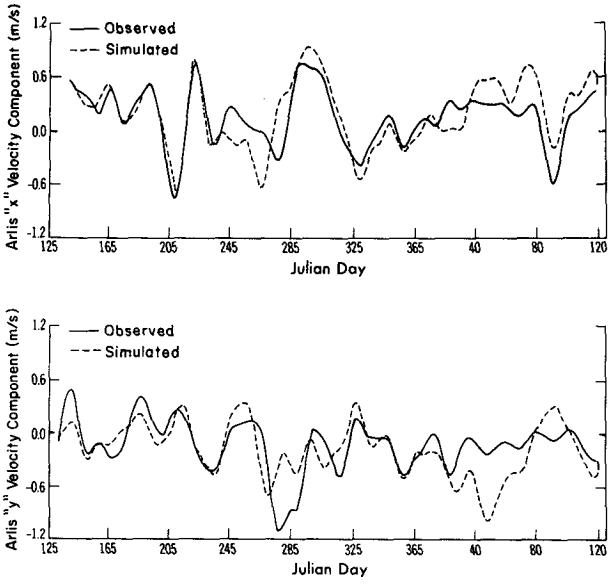

FIG. 14. Simulated (dashed) and observed (solid) 11-day averaged drift rates of Ice Island *Arlis*.

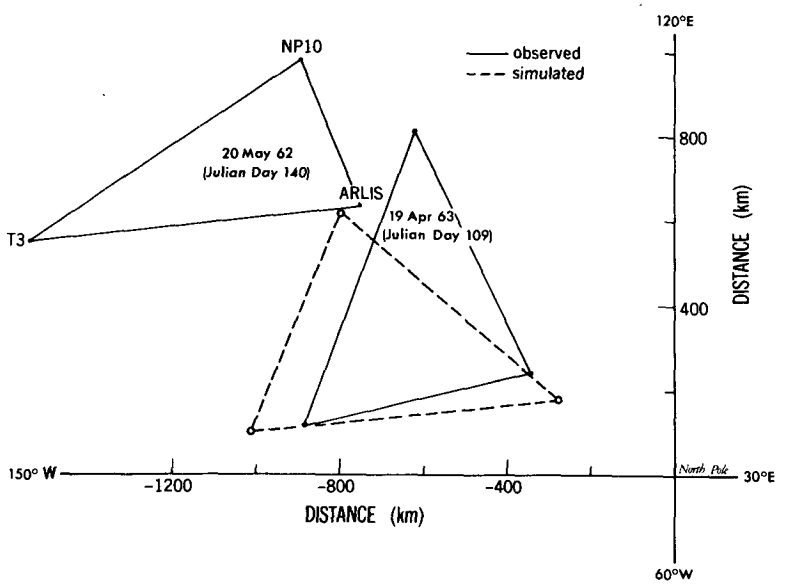

FIG. 15. Observed and simulated cumulative displacement of drifting ice stations over a 334-day interval.

mechanistic models it is necessary to introduce empirical seasonally varying strength parameters. The important point here is that the results in Figs. 14 and 15 are obtained using a physically reasonable simulation model with only two free strength constants, which, once chosen, do not change in time. The seasonal variations of the ice strength (as well as more rapid variations, say in the shear zone) are thus part of the simulated results and do not have to be inserted in an ad hoc manner.

c. *Ice thickness characteristics*

While the ice velocity characteristics can be obtained using shorter simulations, the ice thickness characteristics are a unique feature of a simulation carried out to seasonal equilibrium. Examination of these ice thickness results provides, in many ways, a more discriminating test of the model. One of the most notable results of this model is the simulated geographical variation in thickness due to the ice dynamics. This variation is illustrated in Fig. 16 which shows the average ice thickness contours for April (a month when the pack ice is close to its maximum thickness). Although the thicknesses very near shore may be a bit large, the general form of the contours in the western Arctic Basin is well documented; it also compares favorably with ridging observations. In Fig. 17, for example, are shown values and contours of ridging intensity (a parameter approximately proportional to the volume of deformed ice) taken from laser profilometer data statistics (Hibler *et al.*, 1974a). These contours show heavy ridging off the Canadian Archipelago, which rapidly decreases as one approaches the Pole. Also, recent British submarine sonar measurements (Wadhams, 1979) have shown ice over 6 m thick very near the north coast of Greenland, with thicknesses decreasing to less than 4 m at the Pole.

Probably the best data for estimation of basin-wide ice thickness characteristics are under-ice submarine sonar profiles. Although there have been considerable basin-wide data taken, relatively few have been analyzed methodically. The primary exception to this [besides British submarine data near the Pole (Williams *et al.*, 1975; Wadhams, 1979] are submarine data taken from the 1960 winter cruise of the *Sargo* and the 1960 and 1962 summer cruises of the *Seadragon*, portions of which were reported on by LeSchack *et al.* (1971). Results from selected 8 km sections of these data are shown in Fig. 18 (LeSchack, private communication). These values were obtained by averaging the thickness of the ice-covered portions of submarine tracks of at least three 8 km sections within the same 300 km square region.

Comparison of Figs. 16 and 17 show the simulated geographical variations in ice thickness to be in good agreement with the submarine sonar estimates. The general pattern in both cases, is very thick ice off the Canadian Archipelago with thinner ice off the North Slope and Siberian coast. The primary differences are in the magnitudes of the thicknesses, with the simulated values being higher than observations near Greenland, and smaller near the North Slope and Siberian coast.

It is notable that both these observed and simulated thickness contours are in contrast to seasonal simulated results by Parkinson and Washington

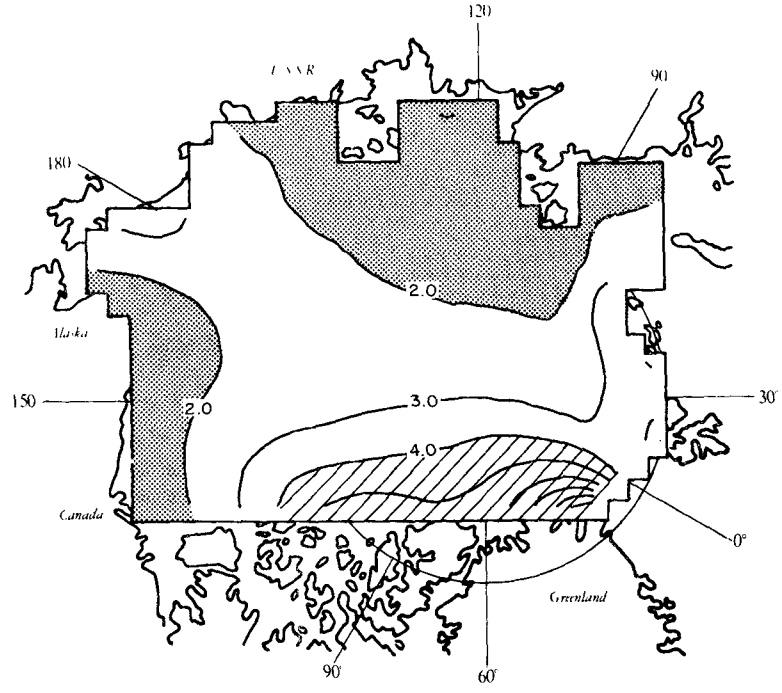

FIG. 16. Simulated average April ice thickness contours. Thicknesses >4 m are shaded by diagonal lines and thicknesses <2 m are denoted by dots.

(1979), who, to a limited degree, also include transport effects. In particular for the Arctic Basin, Parkinson and Washington (1979) obtain results differing very little from thermodynamic considerations alone (see, e.g., Washington *et al.*, 1976), namely, generally thicker ice near the Pole with thinner ice near the coasts, including the Canadian Archipelago.

With respect to compactness, except for a few nearshore regions which may have up to 10% open water for short periods of time, the simulated fall, winter and spring compactnesses are greater than 95%. This is in general agreement with submarine observations in 1960 indicating less than 1.5% open water in the central basin in winter (Wittman and Schule, 1966). However, in summer the compactness decreases, especially in the North Slope and Siberian coast regions. In Fig. 19 are shown the simulated average August compactness contours, together with the average August thickness contours.

These August concentration values are similar to observed ice conditions for relatively ice-free summers on the North Slope. In a historical study of nearshore ice characteristics off the Alaskan coast, Barnett (1979) found 1962 to be a relatively ice-free summer. Ice charts for the summers of 1972 and 1973, which were also "good" summers for navigation, are shown in Fig. 20. The 1972 chart, representing ice conditions on 14 August, was compiled by the Navy Fleet Weather Facility and covers only the North Slope and the Siberian coast. The 1973 chart, representing ice conditions at the end of August, was compiled by the British Meteorological Office at Bracknell and is more complete. Both charts make extensive use of satellite imagery,

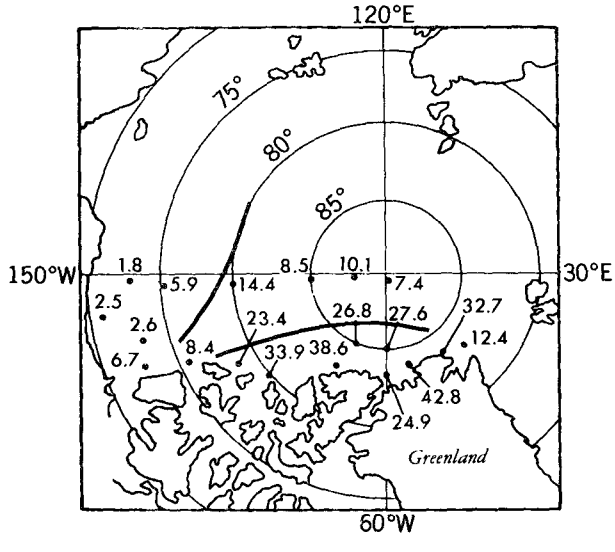

FIG. 17. Ridging intensity (a parameter approximately proportional to the volume of deformed ice) observations and contours obtained from laser profilometer measurements taken during February 1973.

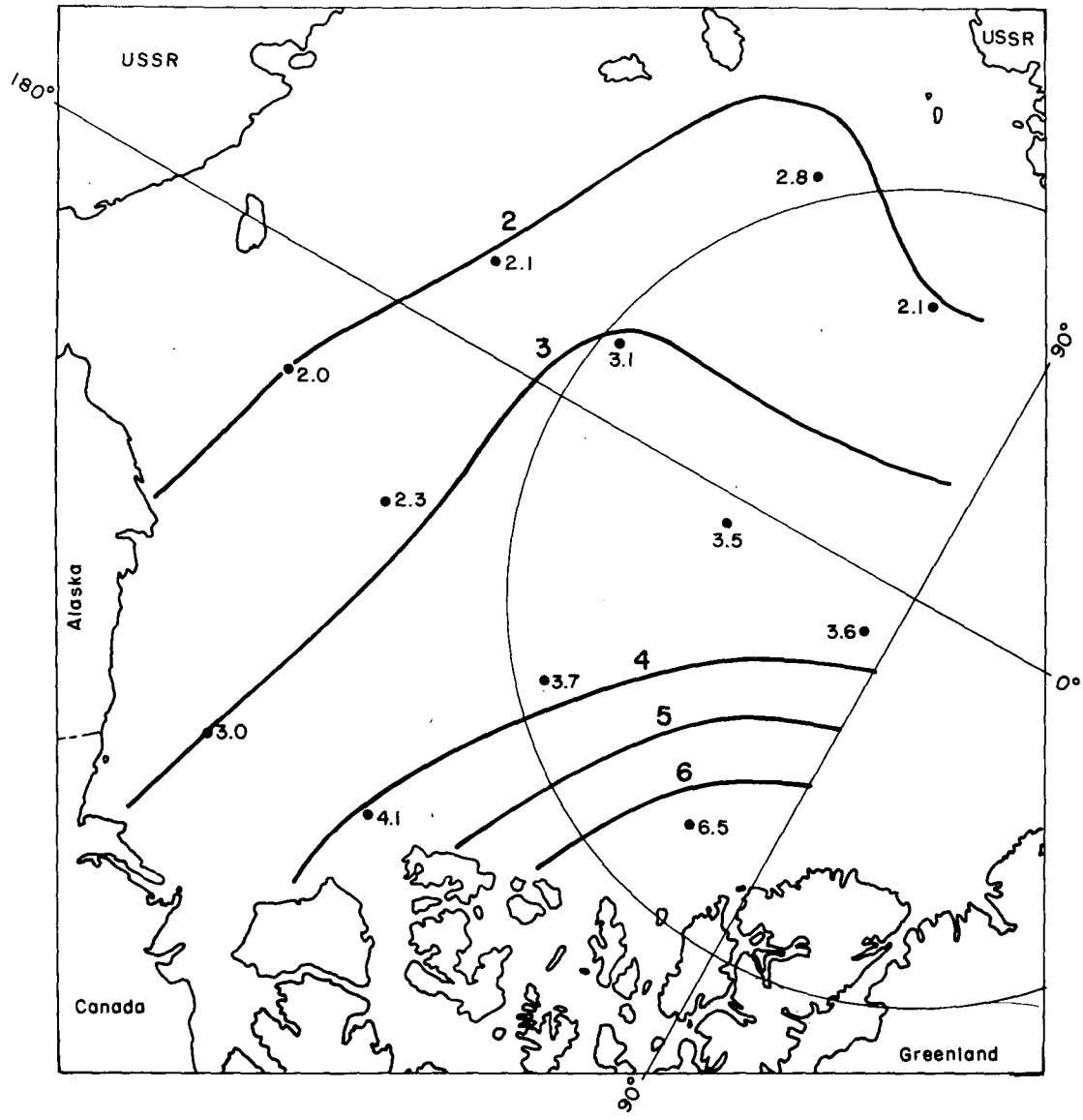

FIG. 18. Contours (m) of observed ice thickness values obtained from submarine sonar data.

including passive microwave cloud-free imagery. (A Bracknell chart is available for 1962 but is based on spotty visual observations and shows little more than an annual mean value similar to the results in Fig. 20.) Comparison of the two charts in Fig. 20 yields some idea of the expected variation of ice edge conditions during "good" summers.

Since the growth rates in the simulation are constant over the basin, the agreement between simulated and observed ice concentration suggests that the nearshore ice conditions in summer are dominated by wind conditions. Such a conclusion is in agreement with the results of an empirical study by Wendler and Jayaweera (1976) who showed that good and bad ice conditions off Alaska correlate well with the 750 mb winds. A noticeable exception, however, is around the Chukchi Sea region. In this region the simulated ice concentrations are much higher than observed. It is likely that this disagreement stems from inadequate thermodynamics in the model [due probably to neglecting northward flowing warm water from the Pacific (R. Paquette, private communication)]. Another difference between simulated and observed results is the lack of totally ice-free regions very near shore. However, it is probable that this effect is partially due to inadequate spatial resolution in the model. It is also likely that there is insufficient melting due, among other reasons, to neglecting the albedo changes caused by the open water.

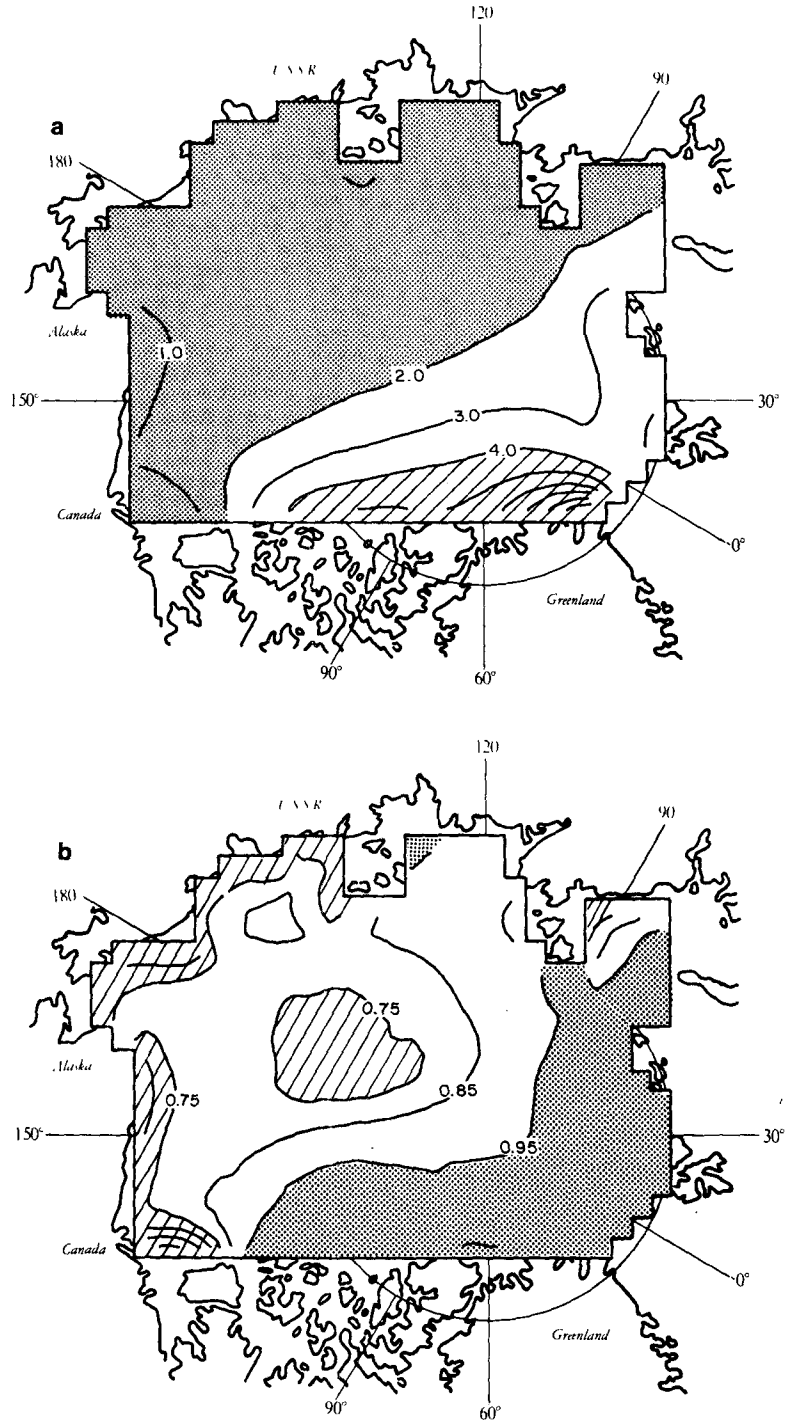

FIG. 19. Average August thickness (a) and compactness (b) contours taken from the standard simulation.

An interesting feature of the simulated August compactness is a large low compactness region far from shore in the vicinity of 80°N, 180°W. Whether or not this is a regular annual feature of the ice concentration is not known. However, there is substantial evidence of such a low compactness region during this specific summer. In particular, Dunbar and Wittman (1963) report that submarine observations in late July 1962 between ice stations T3 and *Arlis* (which were in this region) show ice con-

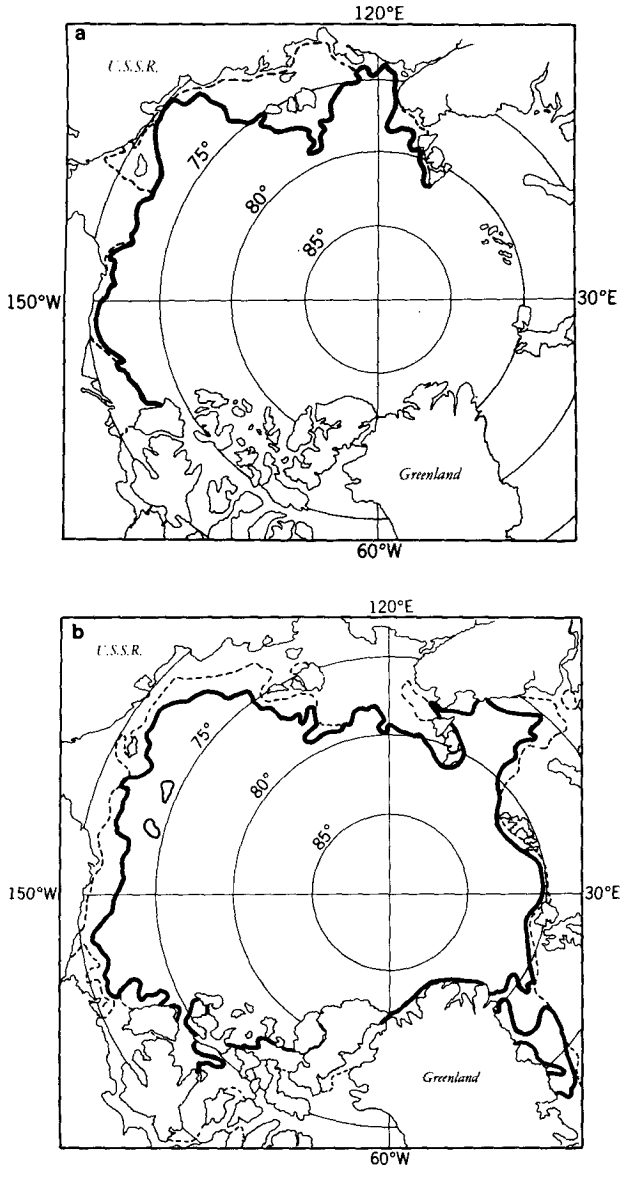

FIG. 20. Observed ice concentration charts for 14 August 1972 (a) and the end of August 1973 (b). The dotted line denotes the edge of the ice-free region whereas the solid line denotes the demarcation between 75% areal ice coverage in (a) and 70% in (b). Chart (a) was taken from the Suitland Fleet weather compilation (no contours are given for Greenland or the Eastern Basin region) and chart (b) from the Meteorological Office, Bracknell, England.

centration of less than 70%. Furthermore, the triangle formed by these two ice stations and NP10 (see Fig. 15), which in August happens to be in the low compactness region, shows a large area increase between the middle of July and the middle of August. Consequently it seems likely that this simulated feature is realistic, but may be an anomaly of this particular summer.

Superimposed on the seasonal variation in ice thickness characteristics are fluctuations, on the scale of days, which are especially pronounced in the nearshore regions. This effect is illustrated in Fig. 21, which shows ice thickness and compactness variations at three nearshore grid cells and three offshore cells. Fluctuations in compactness are especially pronounced in the North Slope region. Thickness changes, on the other hand, are more pronounced in the Canadian Archipelago region. Further offshore these fluctuations are reduced although they are still apparent in the ice thickness records.

Fig. 21 also shows the seasonal ice thickness variation to be more pronounced in the gyre region than in the transpolar drift area. For example, summer–winter thickness variations are ~1 m in the Beaufort Sea and ~0.5 m nearer the Pole. In a calculation based on a moving Lagrangian ice parcel (defined by the same three drifting stations shown in Fig. 15) Thorndike *et al.* (1975) found a similar ice thickness change as simulated in the Beaufort Sea the first year, and a reduced change the second year as the parcel moved toward Spitsbergen. Their results are in general agreement with this simulation.

As a subsidiary effect to the seasonal variation in thickness characteristics, ice strength substantially weakens in summer in most parts of the Arctic Basin. This effect, for two offshore locations, is illustrated by the viscosity time series in Fig. 22. Of particular interest is the decrease in viscosity in the Beaufort Sea in summer, to effectively negligible values which yield free drift conditions. This is consistent with a recent study of summer ice drift based on the 1975–76 AIDJEX data in the Beaufort Sea (McPhee, 1978). McPhee found that the ice drift over approximately the time period Julian Days 200–240 could be well explained by free drift calculations (no internal ice stress).

d. Mass balance characteristics

Although the velocity and thickness characteristics are important for ascertaining the overall validity of this sea ice model, of particular relevance to climatic studies are the mass balance and heat flux characteristics. For a comparison to observations, the average mass balance statistics are calculated and compared in Table 2 with results from an observational study by Koerner (1973). Also, to better illustrate the effects of dynamics on the mass balance, the ice thickness portion alone of the model (without dynamics) is integrated for 20 years and mass balance results tabulated.

In considering Koerner's estimates it should be cautioned that they are based primarily on about

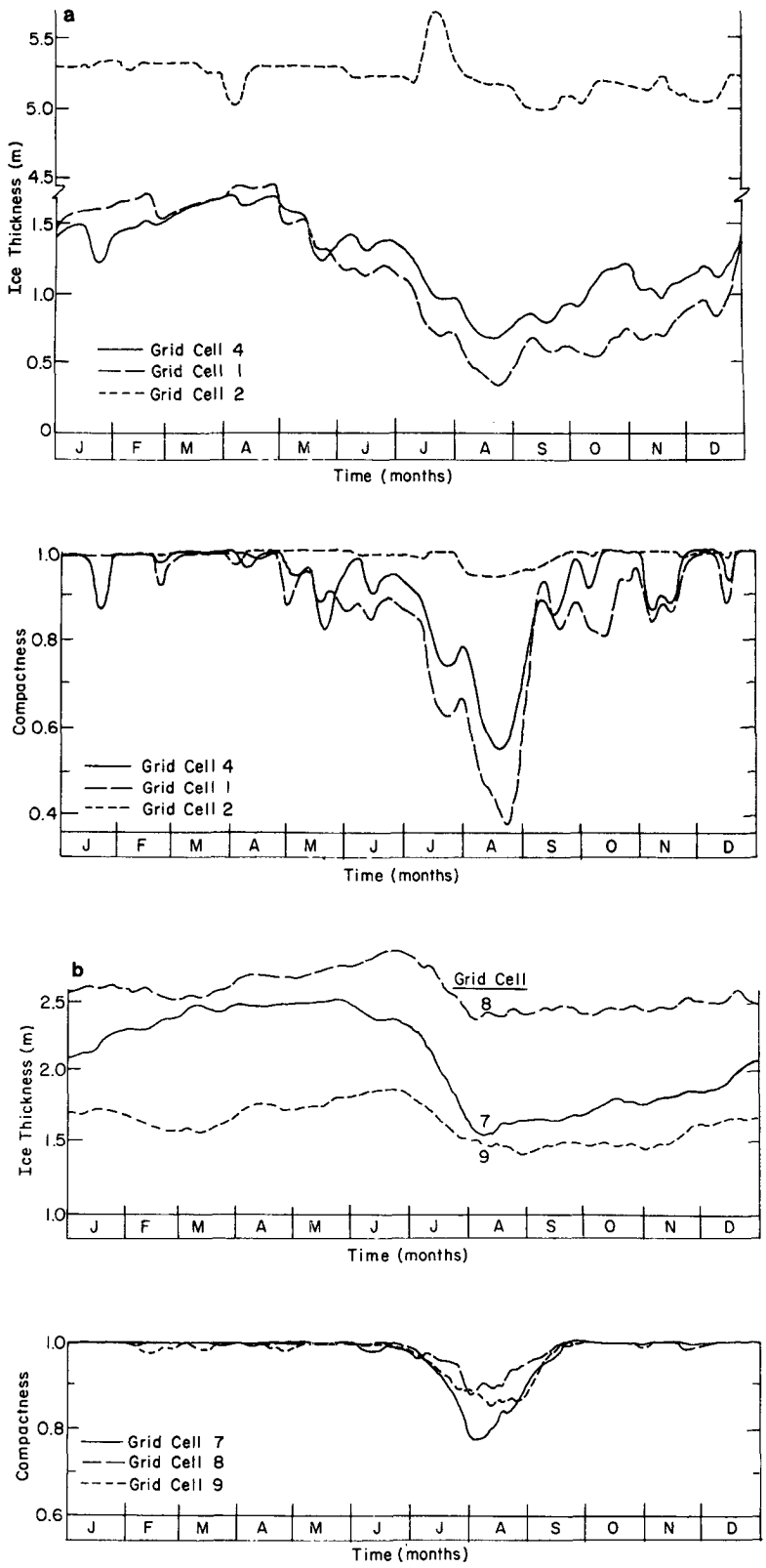

FIG. 21. Nearshore (a) and offshore (b) ice thickness and compactness time series for the eighth year of the standard simulation.

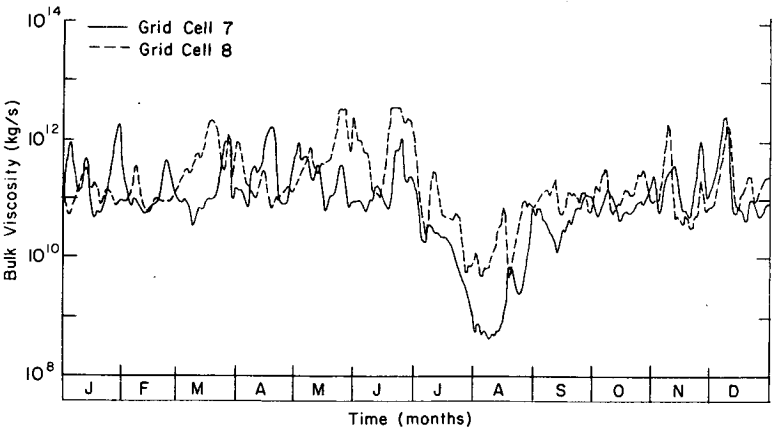

FIG. 22. Offshore bulk viscosity time series. Grid cell 7 is in the Beaufort Sea and grid cell 8 near the Pole.

one year of ground observations taken during the British Transpolar Arctic Expedition (21 February 1968 to 27 May 1969: Barrow to Spitsbergen by dogsled); in addition to representing only one year they are also heavily biased toward the western portion of the Arctic Basin.

Overall, Table 2 suggests that the model is reproducing the basic mass balance characteristics reasonably well, especially since Koerner's values are only estimates. [Aagaard and Greismann (1975), for example, estimate the average outflow rate to be about 0.1 Sv, which is much closer to the model results.] The simulated mean thickness magnitude, which is ~1 m less than Koerner's estimate, exhibits probably the greatest deviation from observation. The ice production (total amount of ice formed through freezing) and net growth, on the other hand, are fairly close to estimated values.

A salient characteristic of the ice growth, illustrated by the table, is the large magnitude of the open water ice production, which in the standard simulation is 34% of the total. This is occurring even though the average percent of open water is less than 3%. Part of this effect is due simply to the fact that the growth rate for open water and thin ice are orders of magnitude larger than thick ice. For example, in January open water is growing at about 12 cm day^{-1}, while 2 m thick ice grows at 0.31 cm day^{-1}. However, a second effect is that the open water will freeze in early fall while thick ice is still melting. Basically the idea is that the thick ice reduces heat loss to the relatively warm atmosphere so that heat from below the mixed layer tends to warm up the mixed layer and melt ice. To illustrate this effect, Fig. 23 shows time series of the basin-averaged open water growth rate and total growth rate. Note the sharp rise in the open water growth in the fall, which is also reflected in the total growth. This effect is also present to a much lesser extent in the dynamics-free case, where the ice melting creates a small amount of open water in the summer (~5%). This fall peak in the growth, however, does not have a pronounced effect on the mean thickness, partially because the mean thickness is constantly being affected by outflow.

TABLE 2. Basin-averaged annual mass balance statistics.

	Outflow	Total ice production (m)	Open water ice production	Average percent of open water	Net growth (m)	Mean maximum ice thickness (m)	Seasonal ice thickness change (m)
Standard simulation	3220 km^3*	0.891	0.299 m (34% of total)	2.84	0.422	2.659	0.524
No dynamics simulation	0.0	0.350		0.54	0.0	3.880	0.350
Koerner's estimates	5580 km^3*	~1.1	~40% of total for ice <1.0 m thick	—	~0.5	~3.7	~0.6

* 3154 km^3 $year^{-1}$ = 0.1 Sverdrup.

While having some seasonal variation, the outflow time series (also shown in Fig. 23) responds primarily to wind fields, as illustrated by its fluctuating character. It is also possible for inflow to occur into the basin under certain conditions, although such effects were relatively small for this simulation. Such a fluctuating outflow is commensurate with observations by Vinje (1976) which indicate that the instantaneous outflow rate may vary from effectively zero to more than twice the mean value.

The thickness time series in Fig. 23 graphically illustrates the marked reduction in the mean ice thickness due to including dynamics in the simulation. The rather small thickness simulated by the coupled model is probably partially due to insufficient detail in the ice thickness distribution. In particular, while the two-level thickness distribution used here keeps approximate track of thin ice up to ~0.5 m, it does not provide much detail on the thicker ice. Consequently, due to the nonlinear nature of the ice growth rates, the mean growth rate of the thick ice could well be larger than the growth rate of level ice having a single mean thickness. This argument is made more compelling by the skewed nature of observed ice thickness distribution (see, e.g., Wadhams, 1979). It is also possible that growth rates are too low due to inadequate amounts of open water being simulated. This could be partially due, for example, to not allowing open water to form under shearing conditions.

In addition to the basin-averaged values, the geographical variations of the ice production are also of some interest. The simulation results show the ice production to be highly concentrated at the boundaries of the basin where the greatest amount of open water and thin ice is being created due to advection. In regions of ice convergence, on the other hand, thick ice is created which tends to ablate even in winter, causing a net negative growth. These effects are illustrated in Fig. 24, a contour map of the annual net growth of ice in meters. At locations of high offshore advection, say off the Canadian North Slope, the net growth exceeds 2 m. It would seem reasonable to infer that such intensified localized growth must have some effect on the Arctic climate and Arctic Ocean circulation.

e. Sensitivity of simulation results to parameterization

Of the parameters in this model, three (P^*,e,C) are strength parameters and one (h_0) characterizes thermodynamic heat loss through thin ice. While changes in these parameters have been found to cause some quantitative modifications in the simulation results, they do not drastically alter the general characteristics described above. To identify the contribution of the different parameters a series of two-year simulations were carried out. In each simulation one constant was varied from the standard value. Although not really equilibrium results, these simulations allow the trend of the effects of the parameters on ice velocity and relative ice thickness to be estimated.

For a methodical examination of the effect of the shape and size of the yield curve on the results (characterized by P^* and e), the major and minor axes of the elliptical yield curve were doubled in length independently. The larger, thinner ellipse has an increased compressive stress P_c (stress occurring under pure convergent deformation—location C in Fig. 2) with smaller changes in the shear stress. The fatter ellipse is just the opposite. In terms of the nonlinear viscosities, increasing the shear-to-compressive-stress ratio is equivalent to increasing the shear viscosity η relative to ζ, the bulk viscosity. For an estimate of the effect of open water on the strength (characterized by the parameter C) experiments were carried out with C doubled.

For a sensitivity study of the h_0 parameter, simulations were carried out with no open water ($A = 1$ always). The $A = 1$ case also effectively represents a simplified version of the model in which only one continuity equation is required, and is comparable to the approach used by Bryan *et al.* (1975) and Manabe *et al.* (1979) to handle the ice thickness although the dynamical interaction is different.

The salient results of the two-year parameter study simulations are given in Table 3 which contains selected heat balance, ice thickness and velocity characteristics. In this table numerical values are given for the second year of the standard case, with percentages (relative to the standard case) given for the sensitivity experiments. The net drift in the table refers to the average simulated drift from day 140 to day 109 of the three drifting ice stations, and the rms velocity refers to an average over the whole grid on day 17. The other parameters are the same as used before or self-explanatory.

The results illustrated by this table can be summarized by the following observations.

1) Increasing the shear strength tends to stiffen the flow in the basin, causing a consequent reduction of outflow and ice drift. However, it does not appreciably affect the relative geographical ice thickness variations.

2) Increasing the compressive strength substantially reduces relative spatial ice thickness variations. Outflow values and drift magnitude, however, change only mildly.

3) Changing the open water strength constant C has only a minimal effect on all characteristics in

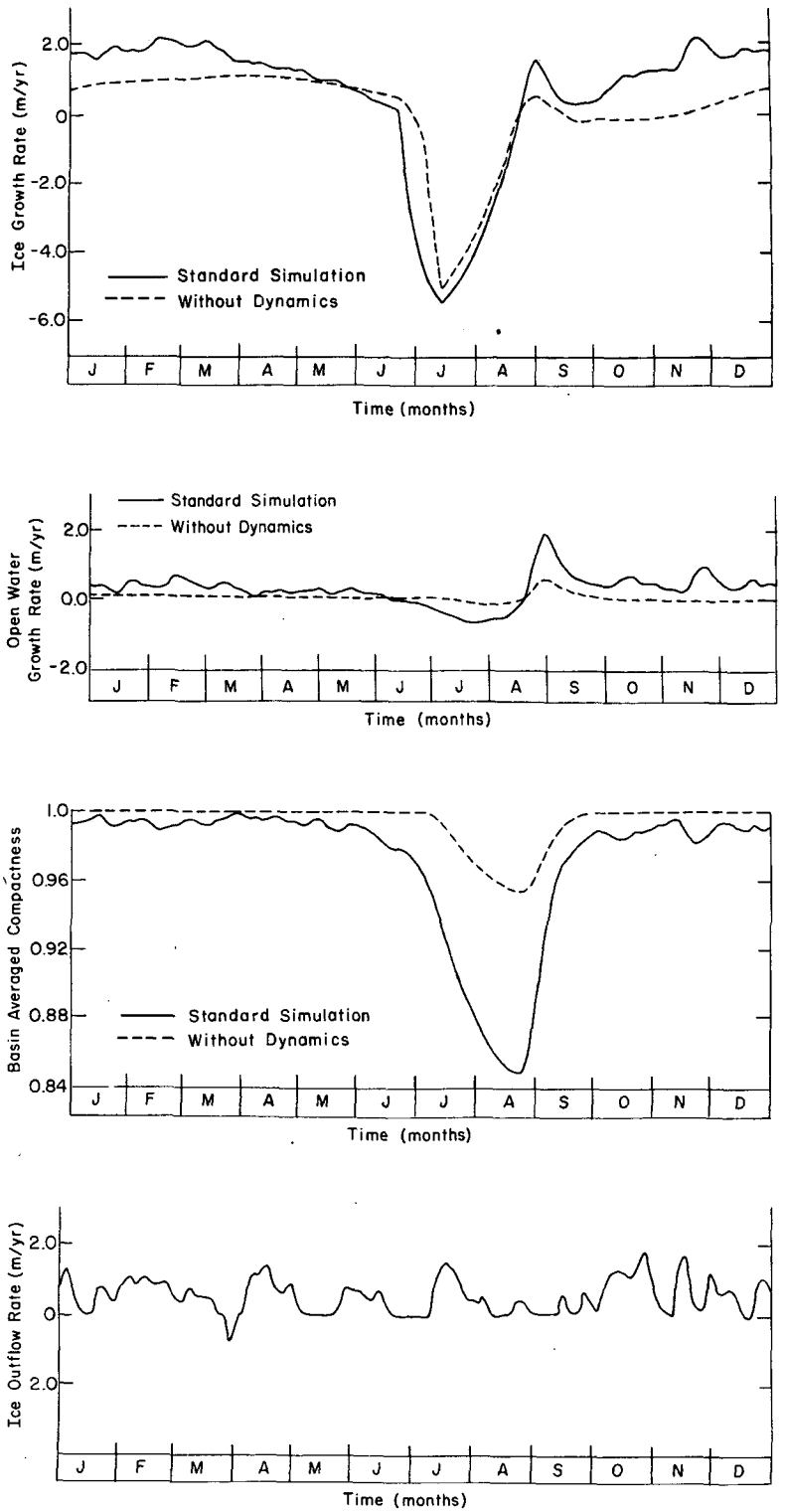

FIG. 23. Basin-averaged mass balance time series for the eighth year of the standard simulation and the no dynamics simulation. Units for the outflow, growth rate and open water growth rate are in meters per year and can be converted to volume of ice by noting that there are 457 grid cells of 125 km by 125 km in the region of the basin modeled here.

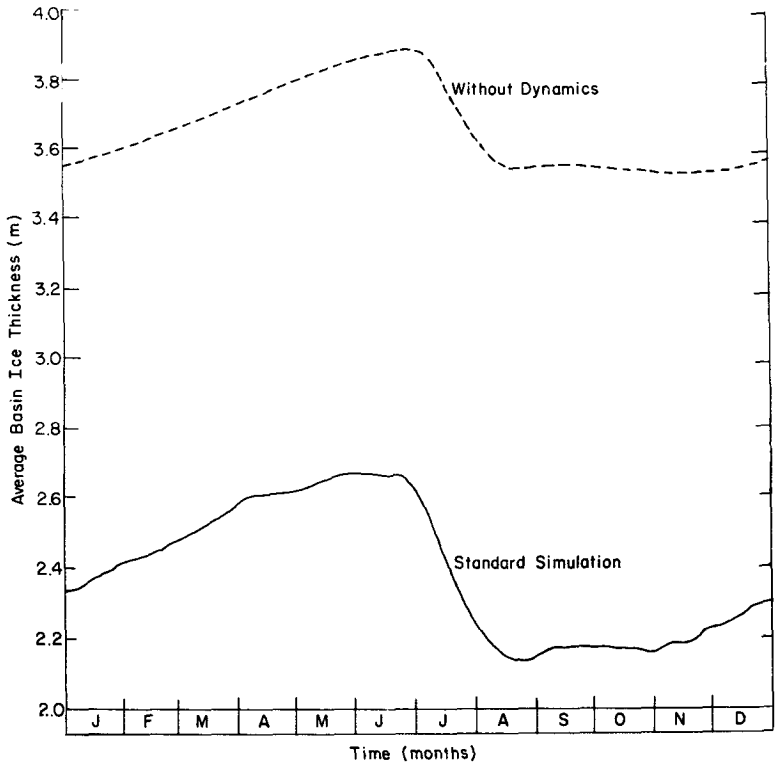

FIG. 23. (*Continued*)

the table. A large C value does, however, cause a greater decrease in ice strength in summer.

4) Removing the open water decreases ice production and mean ice thickness but has little effect on the relative spatial thickness variation and the drift.

In general, these experiments and observations indicate that the yield curve controls the relative geographical ice thickness variations and outflow, while the open water parameterization (h_0) primarily affects the mean thickness and growth characteristics. Rather surprising, however, is the relatively small effect of the open water parameterization (h_0) on the growth and mean thickness. For example, removing the open water entirely only reduces the growth and mean thickness by 10–20%.

To more carefully verify this relatively small effect of the open water parameterization, the simulation with no open water was continued to eight years. Table 4 gives a comparison between the characteristics of this no open water simulation and the standard experiment. The essential effect of removing open water is to reduce the thicknesses and outflow by ~20%. Of some interest is the fact that the ice production is reduced only 5%, reflecting the fact that the increased growth rates of the thinner ice compensate for the absence of open water. It should also be noted that sensitivity experiments similar to those in Table 4 were done with h_0 doubled (i.e., $h_0 = 1.0$). These experiments yielded about a 15% increase in outflow and a 20% increase in thickness. Overall, these sensitivity results suggest that inadequacies in the thermodynamic treatment of thin ice in this model are not causing major changes in the equilibrium thickness characteristics.

4. Concluding remarks

By integrating the sea ice model developed here to a seasonal equilibrium, it has been possible to simulate many of the effects of dynamics on the equilibrium thickness and heat flux characteristics of the Arctic ice cover. Probably the most noticeable effect was a buildup of ice along the Canadian Archipelago in conjunction with a thinning of ice along the North Slope and Siberian coast. As the simulation proceeds in time the buildup strengthens the ice along the Archipelago while the thinning weakens the ice off the other coasts. The resulting strength imbalance eventually counteracts the external forcing thus creating seasonal equilibrium ice thickness and velocity characteristics. A strong

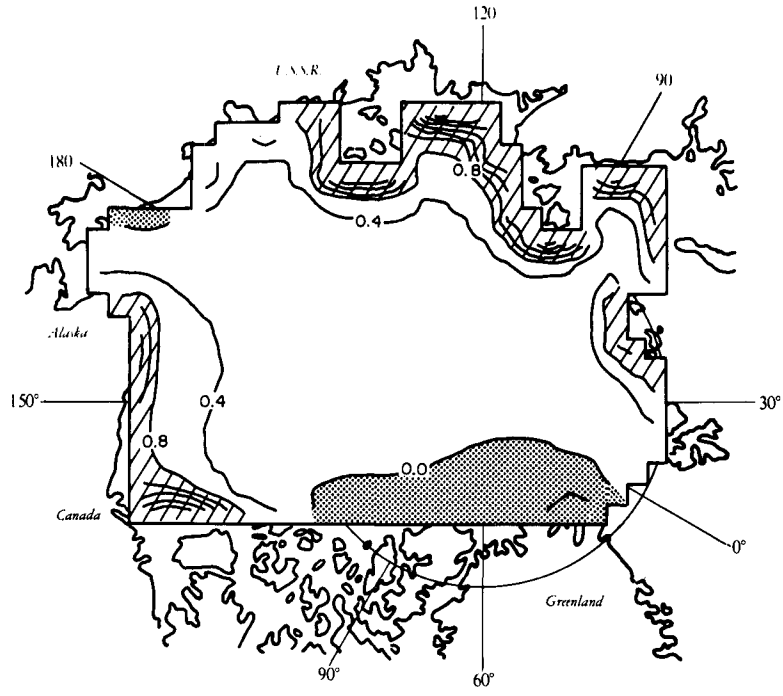

FIG. 24. Year-long net growth contours (at 0.4 m intervals) for the standard simulation.

point of the model is that the thickness contours at which this strength imbalance occurs agree well with observed geographical variations in thickness.

In addition to creating thickness differences the ice transport also causes substantial amounts of open water to form in regions of offshore advection. These effects are particularly pronounced in summer (when open water is not removed by freezing) and result in a region of low compactness off the North Slope and Siberian coast. Further from shore smaller, but still significant, amounts (~10%) of open water also form in summer. During winter conditions, open water formation tends to be mainly limited to short-lived nearshore deformational events. In these events the ice moves away from the coast for a few weeks and then closes up again. Examination of summer ice concentration charts shows the simulated summer compactness effects to be in qualitative agreement with observations. However, quantitative differences exist. Many of these differences appear to be related to spatially varying thermodynamic effects not included in the model. The excessively high simulated summer ice concentration in the Chukchi Sea, for example, is probably due to neglecting the influx of warm Pacific water.

A corollary effect to the offshore ice motion is the strong geographical variation in annual net ice growth (amount of ice grown less the amount melted). In particular, the annual net ice growth is

TABLE 3. Characteristics of two-year sensitivity experiments.*

	Outflow	Ice production	Open water ice production	Average percent of open water	Net drift magnitude	Net drift angle	rms velocity (day 17)	Thickness (day 145, position 3)	Thickness (day 145, position 4)	Average thickness (day 145)	Average thickness (day 241)
Standard	0.493 m	0.702 m	0.256 m	2.30	489 km**	−46°*	0.0513 m s^{-1}	9.132 m	1.885 m	3.314 m	2.836 m
Shear strength doubled	54.0%	82.6%	77.0%	77.8%	72.6%	−44°	06.8%	93.0%	122.0%	105.3%	108.9%
Compressive strength doubled	103.7%	89.5%	77.0%	85.7%	92.8%	−43°	90.8%	65.7%	116.2%	95.4%	94.5%
Open water strength parameter (C) doubled	101.6%	100.7%	100.0%	99.6%	102.1%	−47°	101.4%	100.2%	101.7%	99.8%	99.7%
A = 1.0	95.5%	82.5%	—	—	102.9%	−45°	102.5%	98.3%	83.3%	92.9%	90.8%

* Except for the drift angle, sensitivity results are given in percentages of the standard values (line 1).
** Observed values 562 km; −36°.

TABLE 4. Characteristics of eight-year sensitivity experiments.*

	Outflow	Ice production	Open water ice production	Average percent of open water	Net drift magnitude	Net drift angle	rms velocity (day 17)	Thickness (day 145, position 3)	Thickness (day 145, position 4)	Average thickness (day 145)	Average thickness (day 241)
Standard (8th year)	0.451 m	0.891 m	0.299 m	2.84%	566 km	−49°	0.0569 m/s	8.878 m	1.264 m	2.657 m	2.141 m
$A = 1$	84.7%	94.7%	—	—	105.5%	−50°	105.1%	85.7%	73.9%	83.9%	78.9%

* See first footnote of Table 3.

very large (>1.0 m per year) off the North Slope and Siberian coast. Off the Canadian Archipelago, on the other hand, the net growth is negative reflecting the fact that the ice there is so thick that ablation occurs year-round.

With respect to average basin-wide statistics, the standard simulation yields an annual average outflow rate of ~0.1 Sv in good agreement with observational estimates. This outflow, in turn, causes a net ice growth of 0.42 m annually which occurs in equilibrium in order to balance the ice mass budget. However, less *a priori* obvious changes caused by adding in the dynamics were a 150% increase (as compared to the no dynamics simulation) in the ice production and a reduction (~30%) in the basin-averaged ice thickness. The large ice production (total amount of ice grown) is in good agreement with observed estimates, while the reduced thickness is not. The fact that the ice production increases by an amount greater than the outflow arises primarily from the increased ablation due to the buildup of thick ice along the Canadian Archipelago. Under balance conditions, the total ice growth must balance both the outflow and the increased ablation. The reduction in mean ice thickness, on the other hand, is primarily due to the fact that thinner ice and/or more open water are required to create the increased growth needed to balance the outflow. In the standard simulation the reduced thicknesses required for this (~2.6 m) are rather low compared to observed estimates of 3.5 m. This is in contrast to the dynamics-free simulation which yields about a 3.7 m equilibrium thickness in good agreement with observations.

A possible source of this thickness discrepancy might be reduced growth-rate estimates due to insufficient detail in the ice thickness distribution. While the two-level thickness distribution used here approximately keeps track of ice in the 0–0.5 m range it does not provide much detail on the thicker ice. Due to the nonlinear nature of the ice growth rates it is probable that the mean growth rate of thick ice is larger than the growth rate based on a single mean thickness. Another error source might be inadequate open water formation in winter. In particular, by allowing open water to form due to shear as well as divergence, the ice growth could be increased. Clearly, these considerations emphasize the importance of carrying out simulations along the lines of this study with more detail in the ice strength and ice thickness evolution equations.

Overall, these simulation results illustrate the importance of ice transport on the Arctic heat budget. The effects of this transport are somewhat different from the effects of lead formation due to ice deformation. In particular, the creation of leads primarily modifies the local heat budget while the transport acts, in effect, to move heat laterally. For example, by means of ice transport, heat can effectively be transferred from a portion of the ocean (where ice is melting) to the atmosphere above a different portion (from where the ice is being transported). By constantly transporting ice away from the North Slope region and ultimately out of the Arctic Basin, the dynamics are, in effect, setting up a heat flux from the Greenland sea to the North Slope atmosphere. In the numerical experiments done here the magnitude of this lateral heat flux by ice motion is equivalent to, or larger than, thermodynamic losses without ice motion. Consequently, inclusion of this ice transport in Arctic heat budget studies appears critical. Also, since the ice production is partially a wind-driven effect, it may in many cases respond differently than the thermodynamics to atmospheric conditions. For example, warmer air accompanied by greater cyclonic activity may actually increase ice production due to greater lateral transport even though the local thickness is reduced.

The main objective of this work was to simulate the effects of reasonable ice interaction assumptions on the Arctic sea ice circulation and thickness characteristics. For this purpose, a plastic ice rheology was used in conjunction with a two-level ice thickness parameterization for determining the amount of thin ice in the pack and the strength of the ice interaction. While simple, these parameterizations do capture many features of the variable ice thickness *vis-a-vis* growth and ice strength. Moreover, the numerical experiments described here have been fairly successful in reproducing many of the observed velocity and thickness characteristics of the Arctic ice cover. However, a number of quantitative shortcomings have been noted. It seems likely that many of these shortcomings are due to the idealized treatments made

of the thermodynamics, the coupling of the ice with the ocean, and the ice thickness distribution. Efforts are currently underway to improve these aspects of the model. It is hoped that this study will also provide motivation for similar efforts by other scientists in identifying the role of sea ice in climatic change.

Acknowledgments. I am grateful for the valuable assistance of the staff at the Geophysical Fluid Dynamics Laboratory, with special thanks to Dr. Kirk Bryan and Dr. Syukuro Manabe, whose continued advice and encouragement made completion of this research possible, to Dr. Jerry Mahlman for sharing his insight into the advection problem, to Mr. Mike Cox for discussions on the numerics of ocean modeling, and to Dr. Anthony Gordon for advice on nonlinear instabilities. Comments on the manuscript by Dr. Alan Thorndike and two anonymous referees were also helpful. Finally I would like to thank Dr. J. Smagorinsky for providing me with the opportunity and support to carry out this research. This work was supported by the Office of Naval Research and through Geophysical Fluid Dynamics Laboratory/NOAA Grant 64-7-022-44017.

APPENDIX A

Spatial Finite-Difference Code

1. Momentum equations

In the momentum equations it is necessary to solve by relaxation coupled linearized equations with Dirichlet boundary conditions of the form

$$\lambda v + D_a v - D_s u + F_x + A_1 \partial u/\partial x + A_2 \partial u/\partial y = \tau_x,$$

$$-\lambda u - D_s v - D_a u + F_y + A_1 \partial v/\partial x + A_2 \partial v/\partial y = \tau_y,$$

where $\lambda, D_a, D_s, A_{1,2}$ are spatially varying constants, F_x and F_y are given by Eq. (5) and (6); and τ_x and τ_y are input forcing fields. To obtain finite-difference forms for F_x and F_y expressions are needed for terms of the form $(\eta u_x)_x$, $(\eta u_y)_x$, $(\eta u_y)_y$, $(\eta u_x)_y$, P_y, P_x and similar terms with u replaced with v. (In these expressions x and y subscripts indicate spatial finite differences.) To show the general format it suffices to illustrate the 1st two terms and the last term. Denoting space coordinates by subscripts and using half-integer subscripts for η and P since a staggered grid is employed, the following forms were used for a square grid with mesh size h:

$$\{(\eta u_x)_x\}_{ij} = \frac{1}{2h^2}[(\eta_{i+1/2,j-1/2} + \eta_{i+1/2,j+1/2})(u_{i+1,j} - u_{i,j}) - (\eta_{i-1/2,j-1/2} + \eta_{i-1/2,j+1/2})(u_{i,j} - u_{i-1,j})],$$

$$\{(\eta u_y)_x\}_{ij} = \frac{1}{4h^2}[\eta_{i+1/2,j+1/2}(u_{i+1,j+1} + u_{i,j+1} - u_{i+1,j} - u_{i,j}) + \eta_{i+1/2,j-1/2}(u_{i+1,j} + u_{i,j} - u_{i+1,j-1} - u_{i,j-1}) + \eta_{i-1/2,j+1/2}(u_{i,j} + u_{i-1,j} - u_{i,j+1} - u_{i-1,j+1}) + \eta_{i-1/2,j-1/2}(u_{i,j-1} + u_{i-1,j-1} - u_{i,j} - u_{i-1,j})],$$

$$\{P_x\}_{ij} = \frac{1}{2h}(P_{i+1/2,j+1/2} + P_{i+1/2,j-1/2} - P_{i-1/2,j+1/2} - P_{i-1/2,j-1/2}).$$

Denoting by $(F_{xD})_{ij}$ the finite difference expression for F_x with the diagonal components u_{ij} removed with coefficient D_x (and similarly for $(F_{yD})_{ij}$, the expression for F_y with v_{ij} components—coefficient D_y—removed), the finite-difference equations are solved at each grid point for the superscripted values in terms of the old i values according to

$$\lambda v_{ij}^{i+1} + D_a v_{ij}^{i+1} - D_s u_{ij}^{i+1} + (F_{yD})_{ij}^{i} + D_x u_{ij}^{i+j} + (Au)_{ij}^{i} = \tau_x$$

$$-\lambda u_{ij}^{i+1} - D_s v_{ij}^{i+1} - D_a u_{ij}^{i+1} + (F_{yD})_{ij}^{i} + D_y v_{ij}^{i+1} + (Av)_{ij}^{i} = \tau_y,$$

where $(Au)_{ij}^{i}$ denotes the momentum advection term

$$\frac{1}{2h}[A_1(u_{i+1,j}^{i} - u_{i-1,j}^{i}) + A_2(u_{i,j+1}^{i} - u_{i,j-1}^{i})]$$

and similarly for $(Av)_{ij}^{i}$. The solved equations are then used to replace the old values at position i, j and the sweep continued. Note that at each grid point two simultaneous equations for u_{ij}^{i+1} and v_{ij}^{i+1} must be solved. Without treating the Coriolis terms in this manner the iteration can be shown by a local stability analysis to be unstable for long wavelengths. For an overrelaxation which will normally be faster (but in certain cases can diverge) the old value is replaced by u_{ij}^{1}, where $u_{ij}^{1} = w(u_{ij}^{i+1} - u_{ij}^{i}) + u_{ij}^{i}$ and similarly for v_{ij}. For calculations performed in this paper $w = 1.5$ was found to be useful.

The only other finite differences needed for the momentum equations are strain rate estimates for use in calculating the nonlinear viscosities. These were obtained by an average over the grid cell, e.g.,

$$(\dot{\epsilon}_{11})_{i+1/2,j+1/2} = \frac{1}{2h}[u_{i+1,j+1} + u_{i+1,j} - u_{i,j+1} - u_{i,j}]$$

with similar expressions for the other components.

2. Continuity equations

In the ice thickness equations spatial finite difference of the following terms is required to explicitly integrate the equations forward in time:

$$\partial(uh)/\partial x, \quad \partial(vh)/\partial y, \quad D_1 \frac{\partial^2 h}{\partial x_i^2}, \quad D_2 \frac{\partial^4 h}{\partial x_j^2 \partial x_i^2}.$$

For the advection terms, centered spatial differences identical to those used by Bryan (1969) are employed, *viz.*,

$$[(uh)_x]_{i+1/2,j+1/2}$$

$$= \frac{1}{4h}[(h_{i+1/2,j+1/2} + h_{i+3/2,j+1/2})(u_{i+1,j+1} + u_{i+1,j}) - (h_{i+1/2,j+1/2} + h_{i-1/2,j+1/2})(u_{i-1,j+1} + u_{i-1,j})]$$

and similarly for $(vh)_y$. Since the velocities are zero on the boundaries this automatically conserves mass and can be shown to conserve energy for the incompressible portion of the velocity field. In order to conserve mass for the diffusion terms, the diffusion coefficients are considered to be spatially varying—zero on the boundaries and constant in the interior. The harmonic diffusion term for example is thus properly written $(\partial/\partial x_i)/[D_1(\partial h/\partial x_i)]$ and in finite-difference form is (where for convenience the half integer subscripts have been replaced by integers for the h's)

$$\{(D_1 h_x)_x\}_{ij} = \{(h_{i+1,j} - h_{i,j})D_{1i+1/2,j} - (h_{i,j} - h_{i-1,j})D_{1i-1/2,j}\}$$

with a similar expression for $(D_1 h_y)_y$. For the biharmonic diffusion term, it is considered to be of the form

$$\frac{\partial}{\partial x_l}\sqrt{D_2}\frac{\partial}{\partial x_l}\frac{\partial}{\partial x_p}\sqrt{D_2}\frac{\partial}{\partial x_p}h$$

and is performed by two successive harmonic diffusion operations.

APPENDIX B

Equilibrium Time Scale for the Momentum Balance

In the numerical solution of the momentum equation the nonlinear viscous terms are treated in a semi-implicit manner. In particular, at each timestep an estimate of the velocity field is used to determine the desired viscosities. These estimated viscosities are then used to advance the velocity field to the end of the timestep. Consequently, if, for example, the system is spun up from equilibrium with a constant forcing field using large timesteps,

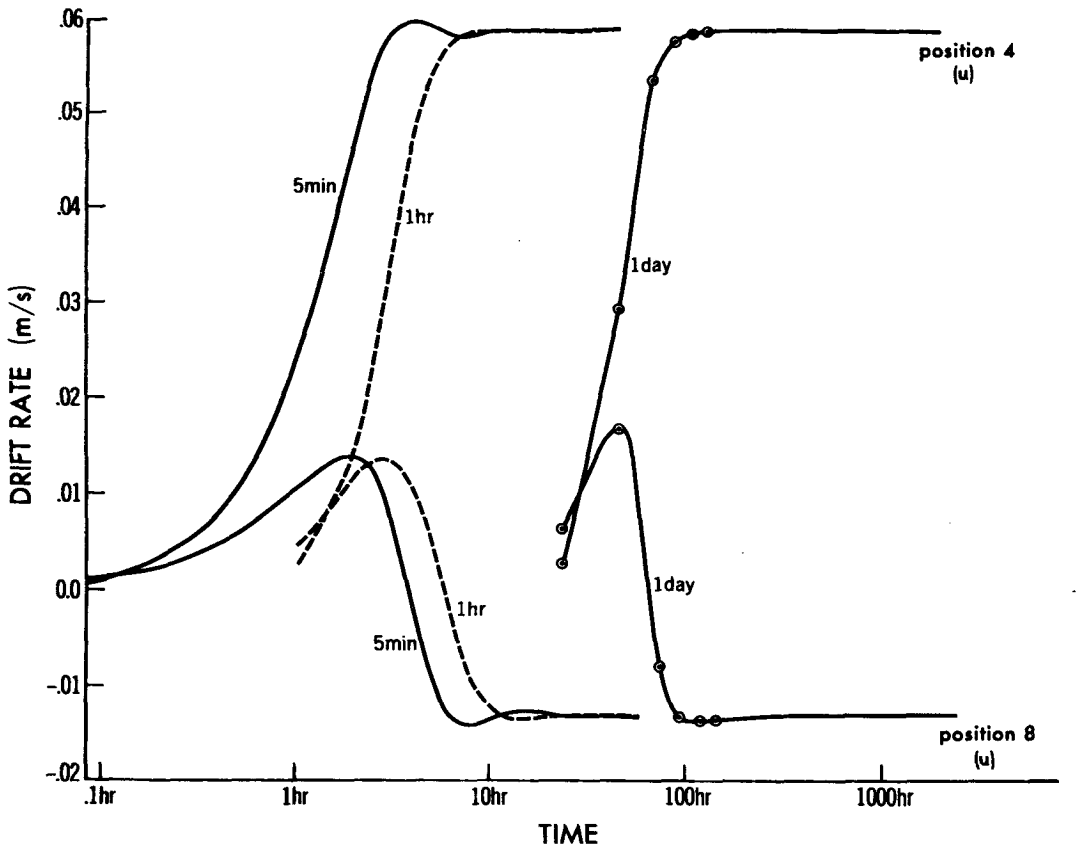

FIG. B1. Approach to equilibrium of the ice velocity using different timesteps in the integration of the momentum equations. In all cases the ice was initially at rest and then a constant wind field turned on. The u component of ice velocity at two selected locations is shown.

even though the inertial terms are negligible, several timesteps will be required to attain equilibrium. Because of this fact timesteps, in practice, should be chosen to be small compared to the scale of temporal variability of the forcing field.

In order to examine the speed of response of the momentum equations as well as the time scales at which inertial effects become important, several integrations of the momentum equations were performed at different timesteps, using a fixed-strength and fixed-forcing fields. In all cases the system was at rest at time zero and a spatially varying but temporally constant wind field then turned on. The grid was the same as that used in the standard simulation (Fig. 6). Resulting velocity values at the circled grid points near grid cells 4 and 8 are plotted versus time in Fig. B1. In all cases the integration was continued for at least 4 days.

As illustrated by the integration at 5 min timesteps, the response of the basin to study state takes several hours and is limited by the inertial terms. (That this response is the true inertial limited response was verified by carrying out an integration at 1 min timesteps with essentially identical results to the 5 min timestep results.) At long timesteps, on the other hand, the inertial terms do not prevent the rapid adjustment of the nonlinear viscosities, and after only about four timesteps the system approaches the same equilibrium velocity state as obtained using small timesteps. For the modeling calculations used in this study, 8-day averaged forcing fields were used. Consequently, 1-day time steps were felt to be small enough to allow adequate adjustment.

APPENDIX C

Velocity Change Due to Ice Thickness Buildup

The time scale for the momentum equation to come to equilibrium is of the order of 1 day, whereas the time scale for thickness equilibrium in the basin is of the order of several years. The time scale for the velocity change due to ice buildup is intermediate between these two and is of the order of weeks.

To illustrate this the grid and parameters used for the standard simulation were used to perform a fixed wind field integration. In particular, a constant geostrophic wind (of magnitude 8.52 m s^{-1}), which yielded a constant surface wind in the negative x direction blowing perpendicular to the boundary along the North Slope, was assumed. Using this forcing field, the coupled system of equations were integrated (using fixed January growth rates) for over a year with initial conditions of a constant thickness of 3.2961 m. Also, to minimize the nonperpendicular motion the Coriolis parameter was taken to be zero and the geostrophic currents neglected. In Fig. C1, the velocity component perpendicular to the North Slope and ice thickness values are plotted versus distance from shore beginning at grid cell 4. Plots are made on days 5, 25, 50, 100 and 200. As can be seen, after about three weeks the velocity nearest shore has dropped to one-fourth of its early value and the thickness has doubled. As the simulation proceeds the edge of the moving pack gradually moves further and further away from shore. Also in the 200 day curve, the thickness far from shore becomes smaller due to the mass of ice in the basin being all stacked up against the shore even though the Greenland-Spitsbergen open boundary outflow condition does allow some ice inflow.

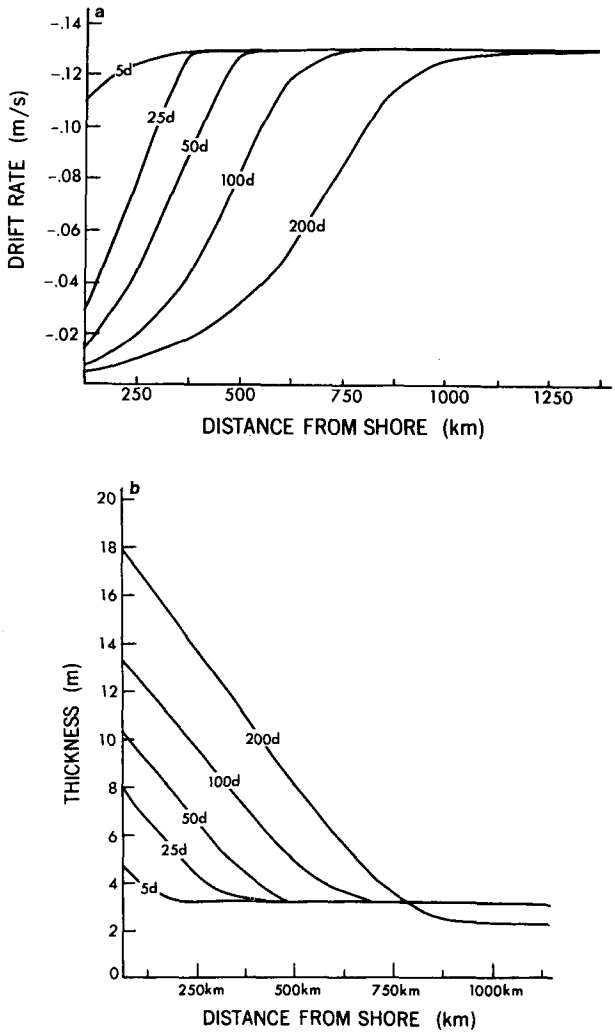

FIG. C1. Ice velocity perpendicular to shore (a) and thickness (b) as a function of distance from shore at various time intervals for a constant onshore wind.

an order of magnitude was carried out with almost identical results being obtained. This indicates both that the diffusion is not affecting the simulation results appreciably and that it could be reduced substantially with no ill effects. One of the reasons for this appears to be that in the complete coupled model the coupling of the strength to the ice thickness equations tends to have effects similar to diffusion since, for example, thin ice regions will be more easily compressed. The diffusion values, on the other hand, were initially chosen based on fixed velocity field advection tests with no dynamic-thickness coupling.

REFERENCES

Aagaard, K., and P. Greisman, 1975: Toward new mass and heat budgets for the Arctic Ocean. *J. Geophys. Res.*, **80**, 3821–3827.

Ames, W. F., 1969: *Numerical Methods for Partial Differential Equations*. Barnes and Noble, 291 pp.

Barnett, D. G., 1979: A long-range ice forecasting method for the North coast of Alaska. *Proc. ICSI/AIDJEX Symp. Sea Ice Process and Models*, University of Washington (in press).

Brown, R. A., 1979: Planetary boundary layer modeling for AIDJEX. *Proc. ICSI/AIDJEX Symp. on Sea Ice Processes and Models*, University of Washington (in press).

Bryan, K., 1969: A numerical method for the study of the circulation of the world oceans. *J. Comput. Phys.*, **4**, 347–376.

——, S. Manabe and R. L. Pacanowski, 1975: A global ocean-atmosphere climate model. Part II. The Oceanic Circulation. *J. Phys. Oceanogr.*, **5**, 30–46.

Campbell, W. J., 1965: The wind-driven circulation of ice and water in a polar ocean. *J. Geophys. Res.*, **70**, 3279–3301.

Coachman, L. K., and K. Aagaard, 1974: Physical oceanography of Arctic and subarctic seas. *Marine Geology and Oceanography of the Arctic Seas*, Y. Herman, Ed., Springer-Verlag, 1–72.

Colony, R., and R. S. Pritchard, 1975: Integration of elastic-plastic constitutive laws. *AIDJEX Bull.*, **30**, 55–80.

Coon, M. D., 1979: A review of AIDJEX modeling. *Proc. ICSI/AIDJEX Symp. on Sea Ice Processes and Models*. University of Washington (in press).

——, S. A. Maykut, R. S. Pritchard, D. A. Rothrock and A. S. Thorndike, 1974: Modeling the pack ice as an elastic-plastic material. *AIDJEX Bull.*, **24**, 1–105.

——, R. Colony, R. S. Pritchard and D. A. Rothrock, 1976: Calculations to test a pack ice model. *Numerical Methods in Geomechanics*. Vol. 2, C. S. Desai, Ed., ASCE, 1210–1227.

Davis, T. M., and A. L. Kontis, 1970: Spline interpolation algorithms for track-type survey data with application to the computation of mean gravity anomalies. Naval Oceanographic Office Tech. Rep. No. 226, 50 pp.

Doronin, Yu. P., 1970: On a method of calculating the compactness and drift of ice floes. *Tr. Arkt. Antartkt. Inst.*, T291, p. 5–17 [English Transl., *AIDJEX Bull.*, **3**, 22–39, 1970].

Dunbar, M., and W. Wittman, 1963: Some features of ice movement in the Arctic basin. *Proc. Arctic Basin Symp., October 1962*. Hershey, Arctic Inst. of North America, 90–103.

Felzenbaum, A. I., 1958: The theory of steady drift of ice and the calculation of the long period mean drift in the central part of the Arctic Basin. *Problemy Severa*, No. 2, 16–46, 1958 [English Transl., *Probl. North*, No. 2, 13–44, 1961].

Gordienko, P., 1958: Arctic ice drift. *Proc. Conf. on Arctic Sea Ice*, Publ. 598, Nat. Acad. Sci. and Nat. Res. Council, Washington, DC, 210–220.

Goodier, J. N., and P. G. Hodge, Jr., 1958: *Elasticity and Plasticity*. Wiley, 152 pp.

Hibler, W. D., III, 1974: Differential sea ice drift II. Comparison of mesoscale strain measurements to linear drift theory predictions. *J. Glaciol.*, **13**, 457–471.

——, 1977: A viscous sea ice law as a stochastic average of plasticity. *J. Geophys. Res.*, **82**, 3932–3938.

——, and W. B. Tucker III, 1979: Some results from a linear viscous model of the Arctic ice cover. *J. Glaciol.* (in press).

——, S. J. Mock, and W. B. Tucker, 1974a: Classification and variation of sea ice ridging in the Western Arctic basin. *J. Geophys. Res.*, **79**, 2735–2743.

——, S. F. Ackley, W. K. Crowder, H. W. McKim and D. M. Anderson, 1974b: Analysis of shear zone ice deformation in the Beaufort Sea using satellite imagery. *The Coast and Shelf of the Beaufort Sea*, J. C. Reed and J. E. Sater, Eds., Arctic Institute of North America, 285–296.

Hunkins, K., 1975: The oceanic boundary layer and stress beneath a drifting ice floe. *J. Geophys. Res.*, **80**, 3425–3433.

Kulakov, I. Yu., M. I. Maslovsky and L. A. Timokhov, 1979: Seasonal variability of Antarctic sea ice extent: Its numerical modeling. *Proc. ICSI/AIDJEX Symp. on Sea Ice Processes and Models*, University of Washington.

Kurihara, Y., 1965: On the use of implicit and iterative methods for the time integration of the wave equation. *Mon. Wea. Rev.*, **93**, 33–46.

Koerner, R. M., 1973: The mass balance of the sea ice of the Arctic Ocean. *J. Glaciol.*, **12**, 173–185.

LeShack, L. A., W. D. Hibler, III and F. H. Morse, 1971: Automatic processing of Arctic pack ice obtained by means of submarine sonar and other remote sensing techniques. *Propagation limitations in remote sensing*, J. B. Lomax, Ed., *AGARD Conf. Proc.*, No. 90, 5-1 to 5-19. [NTIS AGARD-CP-90-71].

McPhee, M., 1975: Ice-ocean momentum transfer for the AIDJEX ice model. *AIDJEX Bull.*, **29**, 93–111.

——, 1979: An analysis of pack ice drift in summer. *Proc. ICSI/AIDJEX Symp. on Sea Ice Processes and Models*. University of Washington (in press).

Manabe, S., K. Bryan and M. J. Spelman, 1979: A global ocean-atmosphere climate model with seasonal variation for future studies of climate sensitivity. *Dynamics of Atmosphere and Ocean* (in press).

Maykut, G. A., 1978: Energy exchange over young sea ice in the central arctic. *J. Geophys. Res.*, **83**, 3646–3658.

——, and N. Untersteiner, 1971: Some results from a time dependent, thermodynamic model of sea ice. *J. Geophys. Res.*, **76**, 1550–1575.

Mesinger, F., and A. Arakawa, 1976: *Numerical Methods Used in Atmospheric Models*. GARP Publ. Ser No. 17, Geneva, 64 pp.

Parkinson, C. L., and W. M. Washington, 1979: A large-scale numerical model of sea ice. *J. Geophys. Res.*, **84**, 311–337.

Pritchard, R. S., 1975: An elastic-plastic constitutive law for sea ice. *J. Appl. Mech.*, **42E**, 379–384.

——, 1978: The effect of strength on simulations of sea ice dynamics. *Proc. Fourth Int. Conf. on Port and Ocean Engineering under Arctic Conditions*, D. E. Muggeridge, Ed., Memorial University of St. Johns, Newfoundland, 494–505.

——, M. D. Coon and M. G. McPhee, 1977: Simulation of sea ice dynamics during AIDJEX. *J. Pressure Vessel Tech.*, **99J**, 491–497.

Reimnitz, E., L. Toimil and P. Barnes, 1978: Arctic continental shelf morphology related to sea ice zonation, Beaufort Sea, Alaska. *Mar. Geol.*, **28**, 179–210.

Rothrock, D. A., 1975a: The steady drift of an incompressible Arctic ice cover. *J. Geophys. Res.*, **80**, 387–397.

——, 1975b: The energetics of the plastic deformation of pack ice by ridging. *J. Geophys. Res.*, **80**, 4514–4519.

Semtner, A. J., Jr., 1976a: A model for the thermodynamic growth of sea ice in numerical investigations of climate. *J. Phys. Oceanogr.*, **6**, 379–389.

——, 1976b: Numerical simulation of the Arctic Ocean circulation, *J. Phys. Oceanogr.*, **6**, 409–425.

Thorndike, A. S., 1973: An integrated system for measuring sea ice motions. *Ocean 73: IEEE Int. Conf. on Engineering in the Ocean Environment*, IEEE Publ. No. 73, 490–499.

——, D. A. Rothrock, G. A. Maykut, and R. Colony, 1975: The thickness distribution of sea ice. *J. Geophys. Res.*, **80**, 4501–4513.

Vinje, T. E., 1976: Sea ice conditions in the European sector of the marginal seas of the Arctic, 1966–1975. *Norsk Polarinstitutt Arbok 1975* (Oslo, 1976), 163–174.

Wadhams, P., 1979: A comparison of sonar and laser profiles along corresponding tracks in the Arctic Ocean. *Proc. ICSI/AIDJEX Symp. on Sea Ice Processes and Models*, University of Washington (in press).

Washington, W. M., A. J. Semtner, C. Parkinson and L. Morrison, 1976: On the development of a seasonal change sea-ice model. *J. Phys. Oceanogr.*, **6**, 679–685.

Wendler, G., and K. F. Jayaweera, 1976: Some remarks on the unusual Beaufort Sea ice conditions in summer 1975. Geophys. Inst. Rep. No. UAGR-246, University of Alaska, 28 pp.

Williams, E., C. Swithinbank and G. de Q. Robin, 1975: A submarine sonar study of Arctic pack ice. *J. Glaciol.*, **15**, 349–362.

Wittman, W. I., and J. J. Schule, 1966: Comments on the mass budget of Arctic pack ice. *Proceedings of the Symp. on the Arctic Heat Budget and Atmospheric Circulation*, Rand Memo. RM-5233-NSF, 215–246. [Available from the Rand Corp., Santa Monica, CA].